Journal of Physics A:
Mathematical and
Theoretical

How boundary interactions dominate emergent driving of inertial passive probes in active matter

OPEN ACCESS
IOP Publishing
Journal of Physics A: Mathematical and Theoretical
J. Phys. A: Math. Theor. **57** (2024) 235006 (31pp)
https://doi.org/10.1088/1751-8121/ad4ad7

How boundary interactions dominate emergent driving of inertial passive probes in active matter

Jeanine Shea[1,*], **Gerhard Jung**[2] and **Friederike Schmid**[3,*]

[1] Technische Universität Berlin, Institut für Theoretische Physik, Hardenbergstr. 36, 10623 Berlin, Germany
[2] Laboratoire Interdisciplinaire de Physique, Université Grenoble Alpes, 38402 Saint-Martin-d'Hères, France
[3] Institut für Physik, Johannes Gutenberg-Universität Mainz, 55099 Mainz, Germany

E-mail: j.shea@tu-berlin.de and friederike.schmid@uni-mainz.de

Received 17 January 2024; revised 2 May 2024
Accepted for publication 13 May 2024
Published 29 May 2024

Abstract

Colloidal probes immersed in an active bath have been found to behave like active particles themselves. Here, we use simulations to investigate the mechanisms behind this behavior. We find that the active motion of the colloid cannot be simply attributed to the convective motion in the bath. Instead, the boundary of the probe contributes significantly to these adopted dynamics by causing active bath particles to spontaneously accumulate at the probe. This gathering of active bath particles then pushes the probe, thus promoting its emergent active-particle-like behavior. Furthermore, we find that the dynamic properties of the probe depend on its size in a non-monotonic way, which further highlights the non-trivial interplay between probe and bath.

Keywords: active matter, non-markovian, nonequilibrium, coarse-graining, tracer dynamics, boundary interactions

* Authors to whom any correspondence should be addressed.

1. Introduction

Many living systems depend on the interplay between active and passive constituents. Important examples include biomixing of fluids and nutrition by microorganisms [1, 2] as well as enhanced transport of mesoscopic particles induced by bacteria and motor proteins [3–5]. To better understand this interplay between passive and active matter, a vast amount of research has been devoted to understanding the dynamics of a passive probe immersed in an active bath both experimentally [4, 6–8], theoretically [9–18], and numerically [19, 20]. A number of these studies have found that a passive probe immersed in an active bath adopts many attributes of active particles themselves [4, 12, 16, 19, 21, 22], therefore indicating universal emergent active behavior. Yet it remains unclear which microscopic mechanism leads the probe to acquire these attributes of an active particle.

The persistent motion of active particles can exert a force perpendicular to the boundary, which accumulates over time and space to generate a 'swim pressure', which represents the pressure exerted by the boundary in order to contain the active particles [23–25]. For boundaries associated with free asymmetric bodies, immersed in the active bath, this swim pressure has been shown to lead to directed motion [13–15, 17, 18, 20, 26, 27]. The situation is more complex for spherically symmetric bodies, such as spherical colloids, which will not exhibit persistent directed motion along some direction which is fixed in the body frame of the particle. However, these symmetric bodies can still experience spontaneous accumulation of active particles at their surfaces which could lead to emergent active propulsion.

Self-propelled particles tend to accumulate at boundaries [28–35]. This accumulation is in part due to complex swimming dynamics of the active particles (e.g. cilia- and flagella-boundary interactions [35] or hydrodynamic interactions [29, 33]) as well as the geometric constraints of the boundary [30, 31]. However, the most simple mechanism for this accumulation is the finite persistence time of active particles, which causes them to maintain their orientation for a finite time even after encountering an obstacle. Importantly, this persistence time is much longer than typical inertial time scales, thus rendering the collisions between active particles and the boundary or colloids inelastic and allowing for accumulation of particles. In some sense, the memory of past motion in the active bath is thus transmitted to the passive probe.

In the present paper, we unravel how the combination of these properties, the accumulation of active particles at boundaries and the directed active motion due to finite persistence time, can lead to spontaneous symmetry breaking and thus to an emergent active behaviour of symmetric passive probes. To determine this mechanism, we consider both impermable and permable spherical passive probes with different radii, immersed in a bath of active Langevin particles (ALPs) [36]. We analyze the inhomogeneous density and orientation of the bath particles in vicinity of the probe and study emergent properties of the passive particle such as its thermal velocity and velocity correlations. Furthermore, we analyze how the memory kernel of the probe changes qualitatively due to the influence of the active bath in driving the colloid out of equilibrium.

We begin in section 3 by examining the active-particle-like behaviors for probes of different sizes. We proceed in section 4 to investigate the properties of the active fluid. In particular, we examine its convective properties in the absence of an immersed probe (section 4.1) and its characteristics in the direct vicinity of an immersed probe (section 4.2). In these sections, we also investigate the influence of probe size on these properties. We summarize and conclude in section 6.

2. Model and simulation details

We consider a three dimensional system of a passive probe immersed in a bath of ALPs of mass m and radius R, which propel themselves with a constant force F_0 subject to rotational diffusion with a diffusion constant D_{R} [19, 36–44]. The ALPs are coupled to a thermal bath with temperature $k_{\mathrm{B}}T$ via a Markovian, Langevin thermostat, and they interact with each other and with the immersed probe by repulsive hard core interactions of the Weeks–Chandler–Anderson (WCA) type [45].

Specifically, we follow references [19, 37, 39, 44] and set the rotational inertia of ALPs to zero for simplicity. The equations of motion for an ALP, n, in the bath, are thus given by

$$m\dot{\mathbf{v}}_n(t) = F_0\mathbf{e}_n(t) - \gamma\mathbf{v}_n(t) + \boldsymbol{\xi}_n(t) - \nabla U_{\mathrm{WCA}}(\mathbf{r}_n - \mathbf{R}) - \sum_{n\neq m}\nabla U_{\mathrm{WCA}}(\mathbf{r}_n - \mathbf{r}_m), \tag{1}$$

where F_0 is the propulsion force of the active particle, $\mathbf{e}(t)$ is the orientation of the active particle, and $\gamma = 6\pi\eta R$ is the damping constant for an ALP radius R in a thermal bath with viscosity η. The term $\boldsymbol{\xi}_n(t)$ represents a stochastic force that mimics implicit collisions of the ALPs with thermal bath particles. These collisions are modeled as Gaussian white noise with mean zero and variance given by a fluctuation-dissipation relation

$$\langle \xi_i(t)\,\xi_j(t')\rangle = 2\gamma k_{\mathrm{B}}T\delta_{ij}\delta(t-t'). \tag{2}$$

The resulting translational diffusion coefficient of isolated ALPs is given by $D_T = k_{\mathrm{B}}T/\gamma$. Finally, the terms $-\nabla U_{\mathrm{WCA}}(\mathbf{r}_n - \mathbf{R})$ and $-\sum_{n\neq m}\nabla U_{\mathrm{WCA}}(\mathbf{r}_n - \mathbf{r}_m)$ in equation (1) describe the WCA interactions with the probe and with all other ALPs, respectively.

The time evolution of the orientation of the ALP, $\mathbf{e}(t)$, is governed by rotational diffusion,

$$\dot{\mathbf{e}}(t) = \mathbf{N}(t)\times\mathbf{e}(t), \tag{3}$$

where $\mathbf{N}(t)$ is again Gaussian white noise with a mean of zero and a variance (another fluctuation-dissipation relation)

$$\langle N_\alpha(t)\,N_\beta(t')\rangle = 2D_R\delta_{\alpha\beta}\delta(t-t'). \tag{4}$$

Here D_{R} is the rotational diffusion constant, which is given by $D_{\mathrm{R}} = 3D_T/4R^2$ for a particle of radius R. The immersed probe only experiences forces from interactions with the surrounding ALPs. Unlike the ALPs, it is not coupled to the thermal bath. In [19], we have shown that the behavior of a probe immersed in an ALP fluid remains qualitatively the same regardless of whether it is coupled to the thermal bath. In particular, the probe acquires an enhanced kinetic temperature which scales quadratically with the activity of the ALP fluid even in the presence of a thermostat.

In the present investigation, we limit ourselves to low Peclet numbers ($\mathrm{Pe} = F_0/(2D_{\mathrm{R}}\gamma R) \leqslant 20$) where MIPS does not occur even for higher densities.

All simulations are performed using LAMMPS [46]. The length, energy, and mass scales in the simulation system are defined by the Lennard–Jones (LJ) diameter σ, energy ϵ, and ALP mass m, respectively, which defines the LJ time scale $t_{\mathrm{LJ}} = \sigma\sqrt{m/\epsilon}$. We use truncated and shifted LJ potentials with the energy scale ϵ which are cut off at $r_{\mathrm{c}} = 2^{\frac{1}{6}}\sigma$, resulting in purely repulsive WCA interactions as described above. The cubic simulation box has periodic boundary conditions in all three dimensions and a side length based on the desired density of the bath.

Table 1. List of probe radii (R_p) investigated as well as their corresponding masses (M), which maintain a constant probe mass to volume ratio of $M/\mathcal{V} = 25/(9\pi)m\sigma^{-3}$.

R_p	M
0.5σ	$0.46296m$
1σ	$3.7037m$
2σ	$29.623m$
3σ	$100.00m$
4σ	$237.04m$

In [19], we have studied a probe of mass $M = 100m$ and radius $R_\mathrm{p} = 3.0\sigma$. We now maintain the mass to volume ratio of the probe from this study — $M/\mathcal{V} = 25/(9\pi)m\sigma^{-3}$ — but change its radius so that the probe has the parameters shown in table 1.

The body of the probe is constructed so that its surface is smooth, resulting in full slip boundary conditions for the LJ fluid. Thus, the bath has no influence on the rotational motion of the probe. The active bath consists of ALPs with a mass of $m_\mathrm{ALP} = 1m$ and a radius of $R = 0.5\sigma$. The number of ALPs in the bath is determined by the desired density of the bath. The parameters of the thermal bath are chosen such that $k_\mathrm{B}T = 1\ \epsilon$ and $\eta = 1\ m/(\sigma t_\mathrm{LJ})$, resulting in $\gamma = 3\pi\, m/t_\mathrm{LJ}$, $D_T = (3\pi)^{-1}\sigma^2/t_\mathrm{LJ}$, and $D_\mathrm{R} = \pi^{-1}/t_\mathrm{LJ}$. The driving force F_0 is varied in the range up to $F_0 \leqslant 50\, m\sigma^2/t_{lJ}$.

In the following, for consistency with previous work [19, 44], we will often also use dimensionless quantities $\hat{t} = t\,\gamma/m$, $\hat{\mathbf{v}} = \mathbf{v}\,\sqrt{m/k_\mathrm{B}T}$, $\hat{F}_0 = F_0\frac{1}{\gamma}\sqrt{m/k_\mathrm{B}T}$, and $\hat{D}_\mathrm{R} = D_\mathrm{R}\,m/\gamma$. Dimensionless quantities will denoted with a hat. Density values and distances are given in LJ units. In these cases, the LJ units are explicitly written with the value.

3. Active-particle-like behavior for probes of different sizes

In earlier work [19], we found that a probe immersed in an active bath exhibits active-particle-like characteristics. Namely, we have found that, from the active bath, the probe inherits a slowly decaying velocity autocorrelation function (VACF), a partially negative memory kernel, and a kinetic temperature which scales quadratically with the bath activity. These are all characteristics shared with active particles themselves.

We additionally find that the mean-squared displacement (MSD) of the probe features a transition from ballistic to diffusive motion, just as it does for an active particle. However, because our probe has inertia, this crossover occurs even in the case of a passive bath (see figure 11(a) in appendix A). Therefore, this crossover cannot be considered as inherently active-particle-like behavior.

To set the stage for the subsequent analysis of boundary interactions, we will now begin with characterizing this active-particle-like behavior in detail for probes of different size.

3.1. Kinetic temperature

We first investigate the difference between the kinetic temperature of the probes in table 1 and that of the bath ALPs ($\Delta k_\mathrm{B}T^{\mathrm{Probe}}_{\mathrm{ALP\ Bath}} = k_\mathrm{B}T_\mathrm{Probe} - k_\mathrm{B}T_{\mathrm{ALP\ Bath}}$). The effective temperature of active matter has been discussed in a number of previous studies [41, 47–50]. However, a unique authoritative definition of non-equilibrium temperature in driven systems far from equilibrium that satisfies thermodynamic requirements is still lacking. Therefore, we choose to use the kinetic temperature, since this is a well defined quantity even for active particles [41].

We define the kinetic temperature of both the probe and a bath ALP as, $k_B T_{\text{eff}} = \frac{m}{d}\langle \mathbf{v}^2 \rangle$, where m is the particle mass, d is the number of dimensions, and $\langle \mathbf{v}^2 \rangle$ is the particle's mean squared velocity [19]. We confirm in appendix B that, for probes of all different sizes, the probe velocity distribution remains Gaussian in an active bath.

In [19], we found that a probe of radius $R_p = 3.0\sigma$ exhibits a higher kinetic temperature than that of the bath ALPs. This is a distinct non-equilibrium signature: in equilibrium, we would expect the probe and bath to thermalize to the same kinetic temperature. Given that our system is out of equilibrium and that we have already seen that the probe kinetic temperature does not necessarily equilibrate to that of the ALP bath, we now analyze how probe size affects kinetic temperature, by characterizing the temperare difference $\Delta k_B T^{\text{Probe}}_{\text{ALP Bath}}$. (In the following, we will often remove the super- and subscripts to make the text more consice.)

As expected in equilibrium, we find that $\Delta k_B T = 0$ for a probe immersed in a passive bath, $\hat{F}_0 = 0$, regardless of bath density and probe size (see figure 1). However, once the bath becomes active, the difference becomes nonzero and depends on both the non-equilibrium driving force and the particle radius. In particular, the behavior of $\Delta k_B T$ as a function of $\hat{F}_0$ for a probe of $R_p = 0.5\sigma$ differs significantly from its behavior for larger probes (compare figure 1(a) with figures 1(b)–(e)). We infer that this different behavior stems both from the fact that, in the $R_p = 0.5\sigma$ case, the probe radius is the same as that of the ALPs themselves and that the mass of the probe is small, i.e. of similar order to the one of the ALPs. Therefore, the probe does not pose a significant obstacle and can be shoved relatively easily by the bath ALPs. This is not the case for larger probes, leading to the different qualitative behavior in figure 1(a).

For all probes with radii $R_p \geqslant 1.0\sigma$, $\Delta k_B T \geqslant 0$ for baths of all densities and activities $\hat{F}_0 > 0$, meaning that the probe is 'hotter' than the ALP bath (see figures 1(b)–(e)). Furthermore, in looking at figures 1(b′)–(e′) where we graph $\Delta k_B T/\hat{F}_0^2$ as a function of $\hat{F}_0$, we can see that $\Delta k_B T$ scales approximately quadratically with $\hat{F}_0$ for probes of all radii $R_p \geqslant 1.0\sigma$. This quadratic scaling of the kinetic temperature difference is the same as was shown for an isolated ALP in [19]. On the other hand, the kinetic temperature difference decreases with increasing bath density, and this again reflects the behavior of the kinetic temperature of the ALP bath itself as a function of density, see [19]: the higher the bath density, the more often the ALP particles undergo random collisions, which effectively slows them down (a bath ALP particle is slower than an isolated ALP). A similar randomization effect seems to govern the interactions with the immersed probe. We will discuss this further in section 4.

In figure 2, we replot the same data as in figure 1, but now showing $\Delta k_B T$ as a function of particle radius R_p, and here, a surprise occurs: for sufficiently high bath activities, the curves are non-monotonic and exhibit a maximum. Such non-monotonic behavior has been seen experimentally for the diffusion coefficient of tracers immersed in bacterial suspensions [51]. It was not, however, observed in the kinetic temperature of the tracers. In appendix C, we calculate the diffusion coefficient of the immersed probe. We do not observe any non-monotonic behavior within the range of parameters that we tested. Instead, the diffusion constants decrease monotonically with increasing particle radius, indicating that the initial increase of the kinetic temperature is more than compensated by the decrease of the particle mobility. However, it does appear that non-monotonic behavior may emerge at higher activities in high density baths. We suspect that whether the non-monotonicity manifests in the kinetic temperature of the probe or the diffusion coefficient is highly dependent on the specifics of the system.

We observe this non-monotonicity of the kinetic temperature for ALP baths of all densities; however, the active force at which the non-monotonicity begins depends on the density. We also

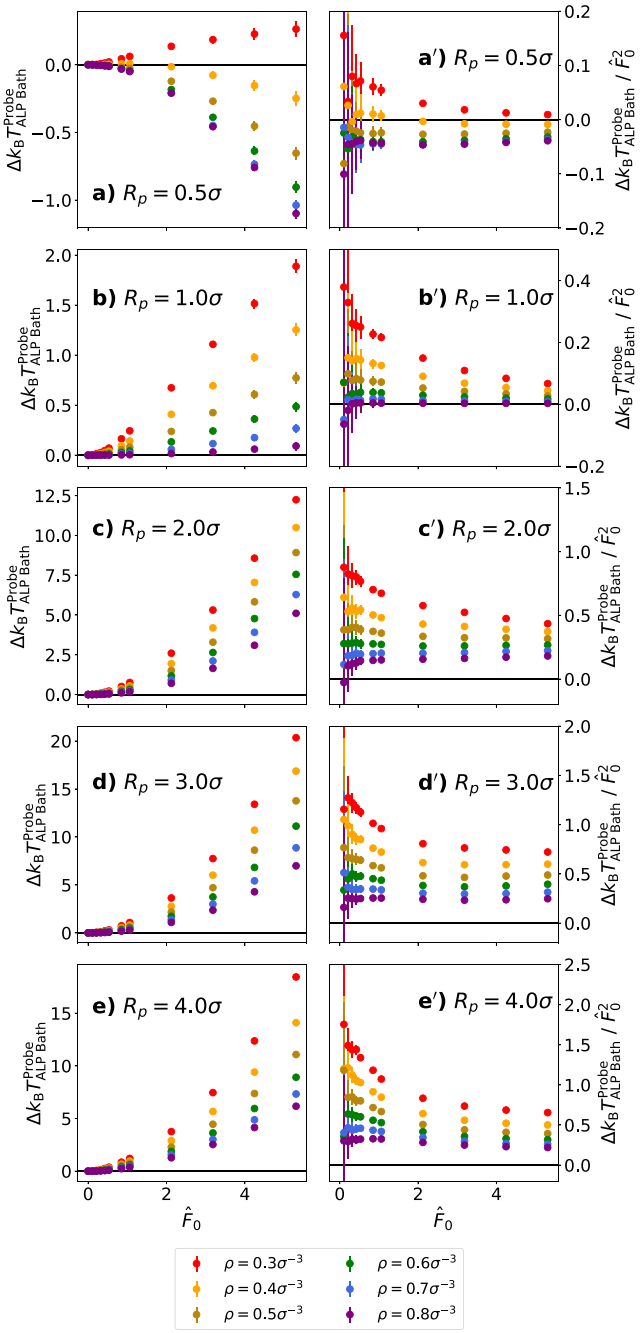

Figure 1. Difference between the probe kinetic temperature and that of a bath ALP ($\Delta k_B T^{\text{Probe}}_{\text{ALP Bath}} = k_B T_{\text{Probe}} - k_B T_{\text{ALP Bath}}$) plotted as a function of the ALP active force ($\hat{F}_0$) for immersed probes with different radii: (a)/(a′) $R_p = 0.5\sigma$, (b)/(b′) $R_p = 1.0\sigma$, (c)/(c′) $R_p = 2.0\sigma$, (d)/(d′) $R_p = 3.0\sigma$, and (e)/(e′) $R_p = 4.0\sigma$. (a)–(d) The left column shows the unscaled difference, whereas (a′)–(d′) the right column shows the difference scaled by $\hat{F}_0^2$. Different colors show different bath densities (ρ). We show a solid black line at 0.

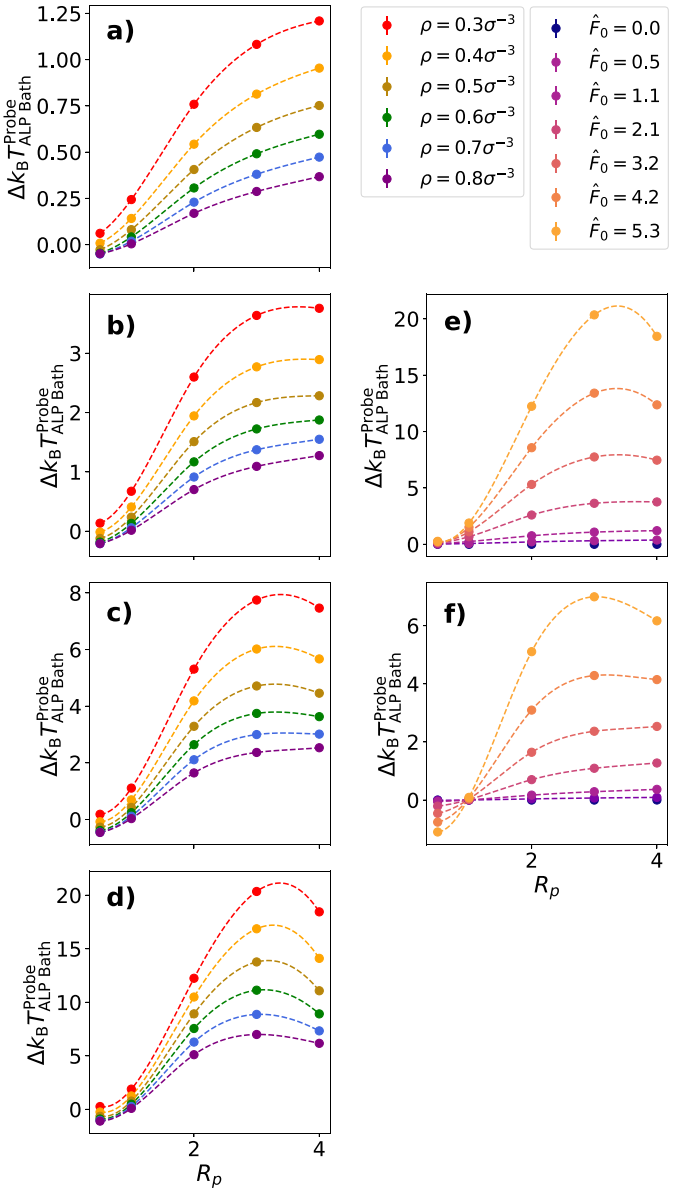

Figure 2. Difference between the probe kinetic temperature and that of the ALP bath ($\Delta k_B T^{\text{Probe}}_{\text{ALP Bath}}$) plotted as a function of the probe radius (R_p). In the left column, each plot shows ALP baths of different densities (ρ, each a different color) for a specific activity ($\hat{F}_0$): (a) $\hat{F}_0 = 1.1$, (b) $\hat{F}_0 = 2.1$, (c) $\hat{F}_0 = 3.2$, and (d) $\hat{F}_0 = 5.3$. In the right column, each plot shows ALP baths of different activities ($\hat{F}_0$, each a different color) for a specific bath density (ρ): (e) $\rho = 0.3\sigma^{-3}$ and (f) $\rho = 0.8\sigma^{-3}$.

see in figure 2 that the maximum value of $\Delta k_B T$ always occurs around $R_p = 3\sigma$, independent of bath density and activity. To better localize the maximum, we fit $\Delta k_B T$ as a function of $\hat{F}_0$ with a spline interpolation (shown as dotted lines in figure 2) and calculate the maximum of

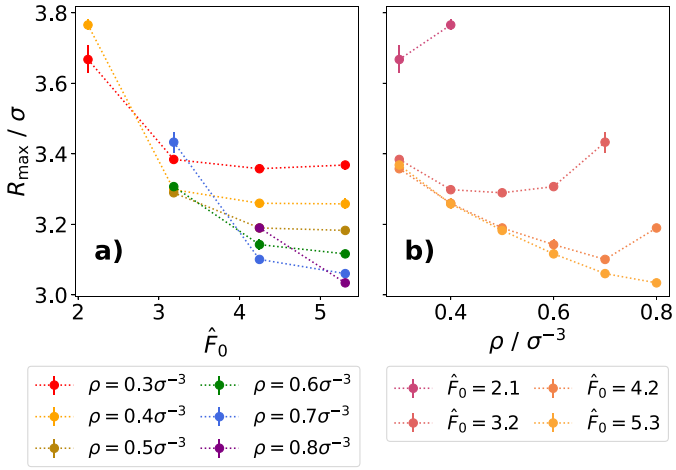

Figure 3. Radius of the probe (R_p) at which $\Delta k_B T$ reaches a maximum as determined by spline interpolation between the data points in figure 2. (a) Maximum as a function of the active force $\hat{F}_0$ where different colors represent different densities (ρ). (b) Maximum as a function of the bath density ρ where different colors represent different activities ($\hat{F}_0$). Densities in the legend are expressed in LJ units of σ^{-3}.

this interpolation (R_{max}), if one exists. The results are shown in figure 3. In creating figure 3, we only consider activities $\hat{F}_0 > 0.2$ because of larger statistical uncertainties in the value of $\Delta k_B T$ for very low activities.

Figure 3 confirms that the non-monotonic behavior (i.e. the presence of a maximum R_{max}) occurs at all densities, but only at higher active forces. For lower active forces, we do not see non-monotonic behavior; however, we cannot exclude the possibility that a maximum may exist beyond our largest studied radius, $R_p = 4.0\sigma$. Figure 3(a) shows that, the higher the density of the bath, the higher the activity necessary for non-monotonic behavior to occur. We also see that, based on our interpolation, that R_{max} slightly depends on both the activity and density of the bath. According to figure 3(a), R_{max} initially decreases with increasing bath activity and then plateaus. The plateau value of R_{max}, approached at high activities in figure 3(a), decreases with increasing density.

The observation of this maximum in the kinetic temperature is unexpected, and the explanation is not obvious. For example, one might suspect that R_{max} is related to a typical distance covered by an ALP at the surface of the probe before the latter reorients. However, in this case it should be correlated with the persistence length of the ALPs, which increases strongly with increasing active force (see appendix D), whereas R_{max} remains roughly constant. Alternatively, one might suspect R_{max} to be connected with the correlation length of collective velocity alignment in the ALP bath. However, as we show in appendix F, the range of these correlations is much smaller than R_{max}. In section 4, we will reconsider this puzzle by analysis of the ALP fluid structure at the probe boundaries.

We conclude this section with the comment that the significant dependence of the probe dynamics on its size provides us with another non-equilibrium signature for a probe immersed in an active bath. In an equilibrium system, we would expect that probes of all sizes would equilibrate to the same kinetic temperature. Therefore, the fact that probes of different sizes

achieve different kinetic temperatures in an active bath can be used as a non-equilibrium signature. In [19], we proposed one non-equilibrium signature of a probe immersed in an active bath which can be determined only from the probe trajectory: the violation of the first fluctuation dissipation theorem. We now propose another non-equilibrium signature of this system which can be determined from the trajectories of differently sized probes: different kinetic temperatures for probes of different sizes in the same active bath. However, this new non-equilibrium signature requires the study of two independent probes of different size and cannot be identified based on one probe trajectory alone.

3.2. VACF and memory kernel

To uncover further active-particle-like properties exhibited by probes of different sizes, we now investigate their dynamic properties. We first focus on the VACF. It has been shown that the VACF of both an isolated ALP and an individual constituent of an ALP fluid decay exponentially with rate $2D_{\mathrm{R}}$ in the limit $t \to \infty$ [19].

For large probes immersed in low activity baths, the values of the VACF in the long time limit are too close to zero to allow for a reliable estimation of decay rates. For small probes immersed in low activity baths and large probes immersed in high activity baths, the VACF decays exponentially at a rate which is very similar to that of the bath ALPs. However, for the case of small probes immersed in high activity baths the decay rate is clearly not the same as that of the bath ALPs: the decay rate is instead higher. We infer that this is due to the fact that the small probes constantly collide with constituents of the active fluid, but do not have sufficient inertia to maintain their current direction. This leads to an effectively lower persistence length of the probe and thereby a faster decay of the VACF. This different behavior of the small probes is not surprising, given the different behavior of the probe kinetic temperature which we already saw in section 3.1.

Thus, at least in certain cases, the probe acquires VACF behavior reminiscent of that of an ALP in the surrounding bath. We now further investigate the dynamic behavior of the probe by mapping its movement onto a generalized Langevin equation (GLE) [52–58]:

$$M\dot{\mathbf{V}}(t) = -\int_0^t \mathrm{d}s\, K(t-s)\,\mathbf{V}(s) + \mathbf{\Gamma}(t)\,, \tag{5}$$

where M is the mass of the probe, $\mathbf{V}(t)$ is its velocity, $K(t-s)$ is the memory kernel, and $\mathbf{\Gamma}(t)$ is the stochastic force on the probe. In mapping the motion of the probe to the GLE, we explicitly allow that the effective dynamics of the colloid in the ALP fluid may be non-Markovian because previous studies have shown that, under certain conditions, the dynamics of a probe immersed in an active bath cannot be assumed to be Markovian [16, 59]. The memory kernel $K(t)$ is determined from the VACF by Volterra inversion, as suggested by the Mori–Zwanzig projection operator formalism [53, 60–64]. We emphasize that the GLE is a coarse-grained model equation, not the true dynamical equation of motion for the probe in the explicit active fluid [19, 44].

In figure 4, we see that the shape of the memory kernel changes qualitatively with increasing activity level in the ALP fluid. It becomes non-monotonous and negative at intermediate times, indicating transient positive feedback that promotes superdiffusive behavior. This is also observed in the memory kernel of isolated ALPs and consistent with our previous findings for a probe of $R_{\mathrm{p}} = 3.0\sigma$ [19]. Although differences between memory kernels of probes with various sizes are clearly visible, the behavior remains qualitatively the same with a short-time

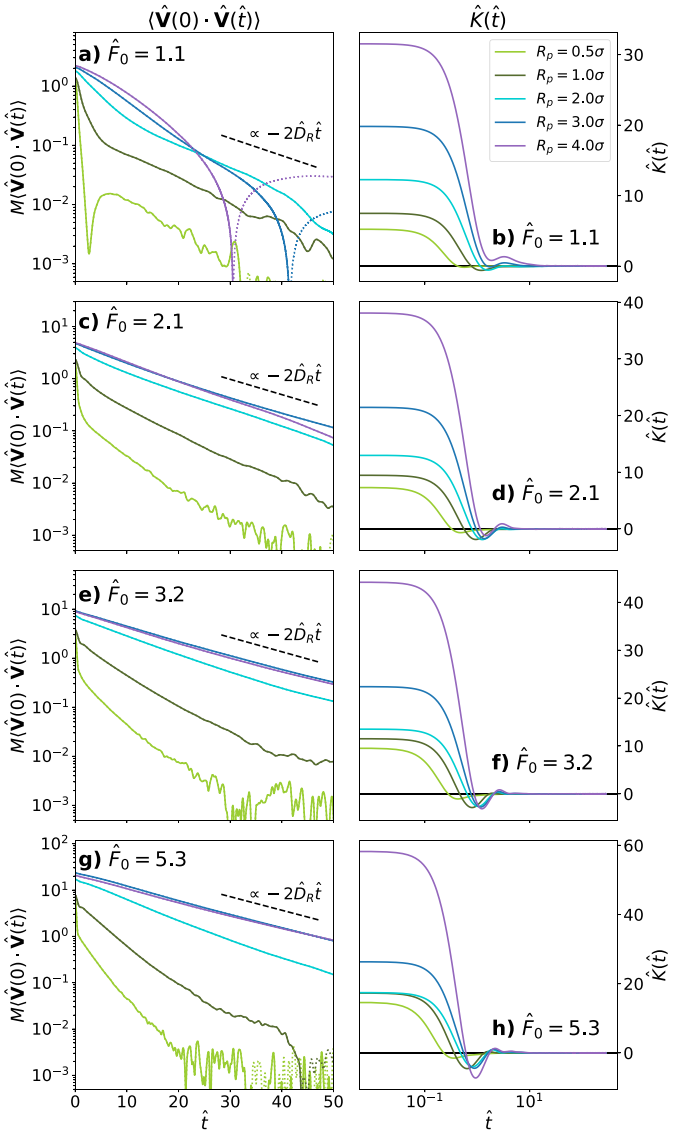

Figure 4. VACF and memory kernel. (a), (c), (e), (g) Semi-logarithmic plot of the VACF for probes of different radii. Each graph shows a different bath activity. Dotted lines show the absolute value of the VACF. (b), (d), (f), (h) Semi-logarithmic plot of the memory kernel for probes of different radii. Each graph shows a different bath activity. The active bath has a density of $\rho = 0.4\sigma^{-3}$ for all cases.

decay and a pronounced minimum at intermediate times for sufficiently high activities. The active force at which this negative portion of the memory kernel first appears is however probe size dependent, as well as its depth. Interestingly, we see in figure 4 that the value of $\hat{K}(0)$ increases monotonically with the radius at all activities. This is in contrast to the initial value of the VACF, which we know—based on the kinetic temperature—becomes non-monotonous for large activities.

4. Characteristics of the active fluid and boundary effects

We have now seen that probes of all sizes $R_\mathrm{p} \geqslant 1.0\sigma$ exhibit active-particle-like behavior in that they exhibit an enhanced kinetic temperature which scales quadratically with the bath activity and their memory kernels indicate transient positive feedback (this behavior of the memory kernel also occurs for $R_\mathrm{p} = 0.5\sigma$). In certain cases, the VACF of the probe also adopts the properties of the surrounding ALP particles. Furthermore, we have seen that the difference between the kinetic temperature of the probe and the ALP bath particles, $\Delta k_\mathrm{B}T$, has a non-monotonic relationship with the probe radius R_p. We now proceed to investigate the mechanism underlying this active-particle-like behavior as well as the cause of the non-monotonic behavior of $\Delta k_\mathrm{B}T$ as a function of the probe radius.

4.1. Convective properties

We have seen that all probes $R_\mathrm{p} \geqslant 1\sigma$ exhibit an enhanced kinetic temperature, which scales quadratically with the bath activity, similar to an ALP itself. But is this active-particle-like behavior purely due to the convective properties of the active bath, or does the interface between the probe and the active bath contribute to this behavior? In order to answer this question, we again consider a bath of ALPs with mass m and velocity $\mathbf{v}_i$ in three dimensions. As stated in section 2, the kinetic temperature of a bath ALP is given by $k_\mathrm{B}T_{\text{ALP bath}} = \frac{m}{d}\langle \mathbf{v}^2 \rangle$, where d is the dimensionality of the system; hence, $\langle \mathbf{v}^2 \rangle = \frac{d}{m} k_\mathrm{B} T_{\text{ALP bath}}$. We now consider a transparent, convective probe particle ('bubble') immersed in the bath (see figure 5). This bubble covers a volume $\mathcal{V} = 4/3\pi R_\mathrm{p}^3$ and swims with the bath ALPs without otherwise affecting them. Namely, if ALPs $j = 1 \ldots N$ are contained in the volume $\mathcal{V}$ of the bubble, then its velocity is $\mathbf{V} = \frac{1}{N}\sum_{j=1}^{N} \mathbf{v}_j$ and its squared velocity is $\langle \mathbf{V}^2 \rangle = \frac{1}{N^2}\sum_{jk}\langle \mathbf{v}_j \mathbf{v}_k \rangle$. In the simplest case, if the ALPs are totally uncorrelated, then $\langle \mathbf{V}^2 \rangle = \frac{1}{N}\langle \mathbf{v}^2 \rangle = \frac{d}{Nm} k_\mathrm{B} T_{\text{ALP bath}}$.

We now assign a hypothetical mass M to the bubble, so that we can determine its hypothetical kinetic temperature, $k_\mathrm{B}T_\mathrm{Probe}$. For the uncorrelated ALP particles, we obtain $T_\mathrm{Probe} = \frac{M}{Nm} T_{\text{ALP bath}}$. For an ALP bath of density ρ, the number of particles contained in volume $\mathcal{V}$ is $N = \rho\mathcal{V}$. Thus, for uncorrelated ALPs:

$$\frac{\rho T_\mathrm{Probe}}{T_{\text{ALP bath}}} = \frac{M}{m\mathcal{V}}. \tag{6}$$

For comparability purposes, we now consider bubbles with the radii and corresponding hypothetical masses listed in table 1. From equation (6), given our ALP mass and the probe mass to volume ratio (which is kept constant as $M/\mathcal{V} = 25/(9\pi)m\sigma^{-3}$ for probes of all radii), we expect that $T_\mathrm{Probe} > T_{\text{ALP bath}}$ for a bubble in a bath of uncorrelated ALPs with $\rho < 1\sigma^{-3}$. This relation is thus qualitatively consistent with the results in [19] and section 3.1 for a hard probe. Therefore, without further investigation, it could be inferred that the hard probe's enhanced kinetic temperature might simply be due to the convective properties of the bath. However, a quantitative inspection shows that the difference $k_\mathrm{B}T$ of the probe and ALP bath temperature greatly exceeds that predicted by equation (6).

On the other hand, our ALPs are not necessarily uncorrelated. To assess the correlations within the ALP bath, we calculate $\Lambda_\mathrm{Bubble} \equiv \rho T_\mathrm{Probe}/T_{\text{ALP bath}}$ for simulations of a transparent, convective probe immersed in an ALP bath. We then compare these values to the theoretical value for a bath of uncorrelated ALP particles (equation (6)) in figures 6(a)–(e).

We first remark that analyzing a bubble of radius $R_\mathrm{p} = 0.5\sigma$ (figure 6(a)) does not provide us with additional insight because, in this case, the volume of the bubble is identical to that of

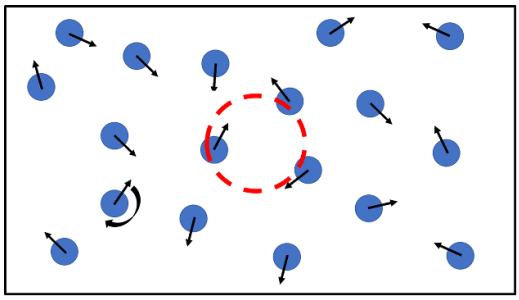

Figure 5. System of a transparent, convective probe ('bubble') immersed in a bath of active Langevin particles.

an ALP. Therefore, the bubble simply tracks a single bath ALP. We thus expect that $T_{\text{Probe}}/M = T_{\text{ALP Bath}}/m$, so $\Lambda_{\text{Bubble}} = \rho M/m = \frac{24}{54}\rho$ for all values of activity, which agrees with our results in figure 6(a).

In figure 6(b), we see that the behavior of a bubble with radius $R_{\text{p}} = 1.0\sigma$ also shows qualitatively different behavior from bubbles with larger radii. We infer that this behavior is due to the small bubble volume. In high density baths, the bubble behavior approaches that of larger bubbles because the bath is sufficiently dense that multiple particles are encompassed within the bubble volume. However, in low density baths, the bubble encompasses, at most times, only one ALP and, consequently, its behavior approaches that of a single ALP.

For bubbles with radii $R_{\text{p}} > 1.0\sigma$ in passive and low activity baths, we find that Λ_{Bubble} calculated from simulation data matches that predicted for a bath of uncorrelated particles (equation (6)) very well, regardless of bath density. This indicates that, in our bath model, for passive and low activity baths, the motion of constituent particles is uncorrelated. However, as the activity of the bath increases, we see that our theoretical model for the bubble underestimates the value of Λ_{Bubble}, indicating that correlations between bath particles emerge with increased activity. These correlations become even more pronounced in higher density baths.

We now assess how the boundary of the probe affects the correlations among bath ALPs by calculating the ratio $\Lambda_{\text{Probe}} \equiv \rho T_{\text{Probe}}/T_{\text{ALP bath}}$ for a hard probe (see figures 6(a′)–(e′)). We consider hard probes with radius and mass parameters listed in table 1. For a hard probe immersed in a passive bath, the probe and bath will be in thermal equilibrium such that $T_{\text{Probe}} = T_{\text{bath}}$; therefore, $\Lambda_{\text{Probe}} = \rho$, as is shown for passive probes of all sizes immersed in passive baths of all densities in figure 6.

Given that, for bubbles of $R_{\text{p}} = 0.5\sigma$ and $R_{\text{p}} = 1.0\sigma$, the bubble often only tracks a single ALP particle, comparing Λ_{Probe} and Λ_{Bubble} for probes of these sizes does not reveal the effects of the probe boundary on probe dynamics. Therefore, we do not discuss a comparison between Λ_{Probe} and Λ_{Bubble} for probes of $R_{\text{p}} = 0.5\sigma$ and $R_{\text{p}} = 1.0\sigma$. We do, however, note that the behavior of Λ_{Probe} as a function of $\hat{F}_0$ for small probes ($R_{\text{p}} \leqslant 1.0\sigma$) qualitatively differs from that which we see for probes of larger radii. We infer that these qualitative differences result from the fact that the probe and the ALPs are on the same length scale.

For all probes with $R_{\text{p}} > 1.0\sigma$, $\Lambda_{\text{Probe}} < \Lambda_{\text{Bubble}}$ for low bath activities. For high bath activities, $\Lambda_{\text{Probe}} > \Lambda_{\text{Bubble}}$. This means that, for low bath activities, the probe boundary *anti-correlates* the bath particles. In the passive case, this anti-correlation is necessary for the probe to come to thermal equilibrium with the bath. For high bath activities, on the other hand, the probe boundary *correlates* the bath particles.

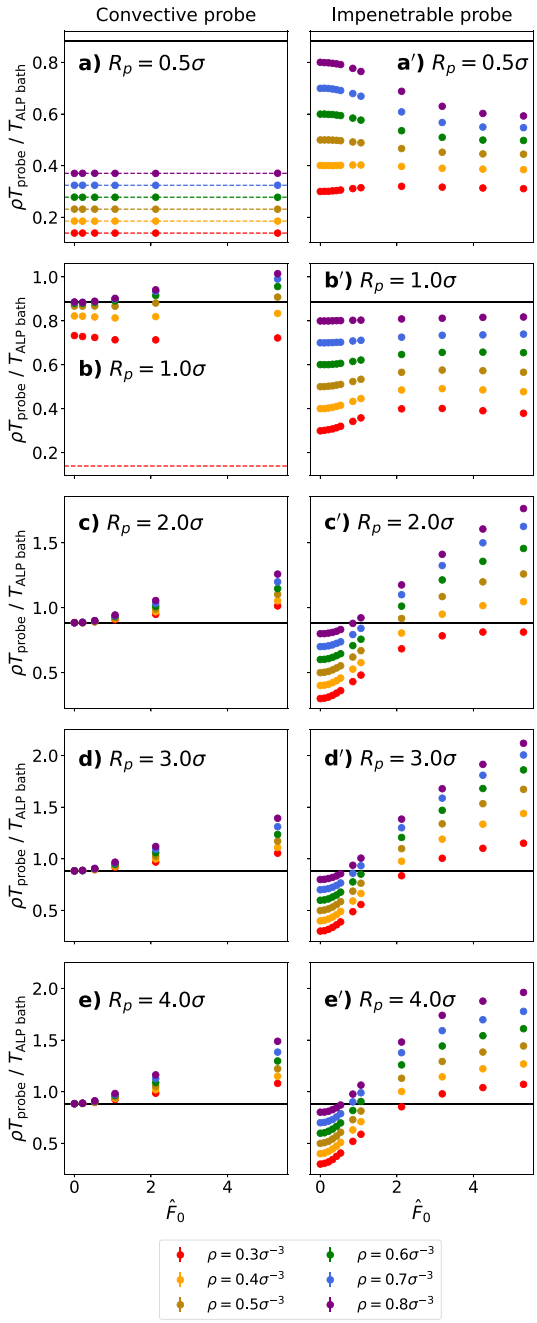

Figure 6. Ratio of the probe temperature (T_{Probe}) to that of a bath ALP ($T_{\text{ALP bath}}$) scaled by the bath density (ρ) and plotted as a function of the ALP active force ($\hat{F}_0$) for immersed probes with different radii: (a)/(a′) $R_{\text{p}} = 0.5\sigma$, (b)/(b′) $R_{\text{p}} = 1.0\sigma$, (c)/(c′) $R_{\text{p}} = 2.0\sigma$, (d)/(d′) $R_{\text{p}} = 3.0\sigma$, and (e)/(e′) $R_{\text{p}} = 4.0\sigma$. (a)–(e) For a transparent, convective probe. (a′)–(e′) For an impenetrable probe with a hard boundary. The solid black line in each graph shows the value predicted for a bath of uncorrelated ALPs (equation (6)). The colored, dotted lines in (a′) show $\rho M/m$. We have also included this line for $\rho = 0.3\sigma^{-3}$ in (b′) for reference.

The most important, if perhaps also most general, conclusion to be drawn from comparing Λ_{Probe} to Λ_{Bubble} is that—for a given bath density, bath activity, and probe radius—they are not the same (i.e. figures 6(a′)–(e′)) are not equivalent to figures 6(a)–(e)). Therefore, the dynamics of the immersed hard probe cannot solely be attributed to the convective properties of the bath. Rather, the probe boundary strongly affects the correlations within the ALP bath, which then influence the probe behavior.

4.2. Properties in the probe vicinity

Given that the probe boundary plays an important role in both the dynamics of the immersed probe and the correlations in the ALP bath, we now examine the properties of the ALP fluid in the vicinity of the probe. We do this for probes of all sizes listed in table 1. We examine the angle-dependent density distribution $\rho(\mathbf{r})$ of ALPs around the probe in a comoving and corotating frame with origin at the probe center, $\mathbf{R}(t)$, and z axis always aligned in the direction of the instantaneous probe velocity $\mathbf{V}(t)$. This method has already been used to study the properties of an ALP fluid surrounding a probe of radius $R_{\text{p}} = 3.0\sigma$ in [44].

To quantify the angular dependence, we expand the density distribution $\rho(\mathbf{r})$ in spherical harmonics,

$$\rho(\mathbf{r}) = \sum_{lm} Y^*_{lm}(\mathbf{r}/r)\, \Omega^m_l(r)\,. \tag{7}$$

The coefficients $\Omega^m_l(r)$ can be determined from simulations according to

$$\Omega^m_l(r) = \frac{1}{\mathcal{V}} \sum_{n\in\delta\mathbf{r}} Y_{lm}(\mathbf{r}_n/r_n)\,, \tag{8}$$

where the sum $\sum_{n\in\delta\mathbf{r}}$ runs over all bath particles in a spherical shell δr around the particle (i.e. their distance from the probe center lies within the interval $[r-\delta r/2 : r+\delta r/2]$), and $\mathcal{V}$ is the volume of the shell, $\mathcal{V}(r) = 4/3\pi((r+\delta r/2)^3 - (r-\delta r/2)^3)$. Specifically, the radial average of $\rho(\mathbf{r})$ can be obtained from

$$\rho(r) = Y^*_{00}\,\Omega^0_0 = \frac{\sqrt{4\pi}}{\mathcal{V}} \sum_{n\in\delta\mathbf{r}} Y^0_0(\mathbf{r}_n/r_n)\,. \tag{9}$$

In [14], it was analytically found that, for a sphere immersed in a dilute 3D system of ABPs, the ABP concentration decays exponentially to the bulk density. We now examine the density profile surrounding a spherical probe immersed in a dense 3D system of ALPs through simulation data. We can see in figures 7(a)–(e) that, even in a bath of density $\rho = 0.4\sigma^{-3}$, our bath is sufficiently dense to show oscillations before approaching the bulk density.

In comparing the density curves for a passive and an active bath in figures 7(a)–(e), we see that the first peak of the density curve is higher in an active bath for probes of all radii. This means that adding activity to the bath leads to a higher density of bath particles in the vicinity of the probe. Interestingly, we see that the magnitude of increase in the peak density is non-monotonic with the probe radius. Similarly to the behavior of $\Delta k_{\text{B}}T$, this difference reaches a maximum for a probe of $R_{\text{p}} = 3.0\sigma$ and then decreases for a probe of $R_{\text{p}} = 4.0\sigma$.

We also see that the initial peak of the active bath density profile is shifted slightly closer to the probe center in comparison with that of the passive bath, again independent of probe

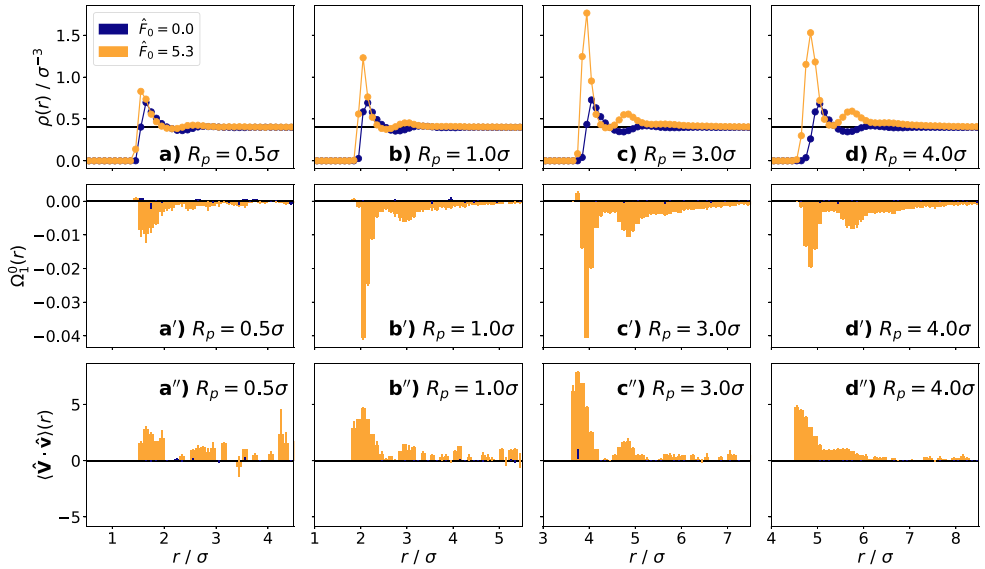

Figure 7. (a)–(d) Density of the bath ($\rho(r)$) in LJ units of σ^{-3}, (a′)–(d′) dipole moment of the bath ($\Omega_1^0(r)$, see equation (8)), and (a″)–(d″) alignment of the ALP velocities with that of the probe velocity ($\langle \mathbf{V} \cdot \mathbf{v} \rangle(r)$, see equation (10)) as a function of distance from the center of the immersed probe (r) for baths of average density $\rho_0 = 0.4\sigma^{-3}$. Each column shows a probe of a different radius: (a)/(a′)/(a″) $R_\mathrm{p} = 0.5\sigma$, (b)/(b′)/(b″) $R_\mathrm{p} = 1.0\sigma$, (c)/(c′)/(c″) $R_\mathrm{p} = 3.0\sigma$, and (d)/(d′)/(d″) $R_\mathrm{p} = 4.0\sigma$. For ease of visualization, in (a)–(d) we show a black line at the global density and in (a′)–(d′) and (a″)–(d″) we show a black line at 0.

radius. Furthermore, the spacing between the first and second shells of the active bath particles are closer together. These closer shells indicate that ALPs are able to move closer to the probe, and each other, than passive bath particles. We infer that this ability stems from the higher kinetic energy of ALPs due to their active force, which allows them to overcome more of the repulsive potential from WCA interactions with the probe.

For a passive bath, the higher order spherical harmonics of the density distribution of the bath are all zero. On the other hand, from figures 7(a′)–(d′), we see that the ALP bath acquires a negative dipole moment surrounding the probe, which is sustained to large values of r. This negative dipole moment indicates that ALPs collect behind the probe relative to its instantaneous velocity, even at large distances from the probe. The phenomenon of active particles gathering behind an immersed passive probe has previously been seen for a probe dragged through an ABP bath in [65], where it is framed as a difference between the forces behind and in front of the probe. In our systems with spherically symmetric probes, we find that the spatial distribution of ALP particles can be fully characterized by the $\rho(r)$ and $\Omega_1^0(r)$. Higher order spherical harmonics of the density distribution did not exhibit structure within the error, neither in the active, nor in the passive bath.

We note here that, as seen in the density profile, the magnitude of the dipole moment peak has a non-monotonic relationship with the probe radius. The small values of $\Omega_1^0(r)$ for a probe of radius $R_\mathrm{p} = 0.5\sigma$ demonstrate that the accumulation mechanism is not significant for a probe

of this size. The failure of this mechanism can be explained intuitively: If the probe has the same size (in volume) as the ALPs themselves and has a correspondingly small mass, significant accumulation is not possible. This lack of accumulation helps to explain why the behavior of $\Delta k_{\mathrm{B}}T$ as a function of $\hat{F}_0$ for a probe of $R_{\mathrm{p}} = 0.5\sigma$ differs significantly from probes with larger radii (see figure 1). Large probes with $R_{\mathrm{p}} = 4.0\sigma$ also have smaller values of $\Omega_1^0(r)$ when compared with probes of intermediate sizes. This can be understood by considering the limit that the size and mass of the probe becomes infinite. In this case, there will also be no net dipole moment because the the particle will not move. Therefore, combining this knowledge of the small and large probe limits, we conclude that there must be a maximum in between, i.e. the magnitude of the dipole moment must exhibit non-monotonic behavior. We will reconsider this question in section 5.

We infer that the velocities of the ALPs collected behind the probe become correlated and effectively *push* the probe. To assess this hypothesis, we calculate the alignment of ALP velocities with that of the probe as:

$$\langle \mathbf{V}\cdot\mathbf{v}\rangle(r) = \frac{1}{\rho(r)}\sum_{i\in\delta\mathbf{r}} \mathbf{V}\cdot\mathbf{v}_i. \tag{10}$$

Figures 7(a′′)–(d′′), confirm that the probe velocity is in fact aligned with the ALPs in its vicinity, supporting our hypothesis of this pushing mechanism. We see in figures 7(a′′)–(d′′) that the height of the maximum peak in $\langle \mathbf{V}\cdot\mathbf{v}\rangle(r)$ has a non-monotonic relationship to the probe radius, much like $\Delta k_{\mathrm{B}}T$ and the maximum of the density peak. The maximum peak of $\langle \mathbf{V}\cdot\mathbf{v}\rangle(r)$ occurs, once again, at approximately $R_{\mathrm{p}} = 3\sigma$.

We furthermore infer that the pushing by the ALPs promotes the enhanced kinetic temperature of the probe and induces its active-particle-like behavior (i.e. its VACF and memory kernel behavior). Indeed, we can see in figure 8 that the kinetic temperature difference between the immersed probe and the ALP bath has a strong positive correlation with the average dipole moment, $\langle\Omega_1^0\rangle$—for small values approximately linearly and for large values approximately quadratically. Here $\langle\Omega_1^0\rangle$ is defined as

$$\langle\Omega_1^0\rangle = \int_{\mathcal{V}_1} \mathrm{d}\mathcal{V}\ \Omega_1^0(r)/(4\pi r^2) \tag{11}$$

where $\mathcal{V}_1$ is the volume corresponding to the first peak in the dipole moment. The integral on the right hand side of the equation was found to be positive in only very few cases for low values of $\hat{F}_0$.

Figure 8(a) shows a double logarithmic plot of the kinetic energy difference between probe particle and bath, $\Delta k_B T$, versus $(-\langle\Omega_1^0\rangle)$. Points where $\langle\Omega_1^0\rangle$ and/or $\Delta k_{\mathrm{B}}T$ are zero within the error are omitted. We note a strong positive correlation between $\Delta k_B T$ and $-\langle\Omega_1^0\rangle^2$ for probes of radii $R_{\mathrm{p}} > 1.0\sigma$. For $R_{\mathrm{p}} = 0.5\sigma$, most values of $\langle\Omega_1^0\rangle$ are close to zero and hence not shown. For probes with $R_{\mathrm{p}} = 1.0\sigma$, we see a cluster of points in the lower right corner of the graph. The location of this cluster indicates that, in spite of high values of $\langle\Omega_1^0\rangle$, $k_{\mathrm{B}}T$ remains low. We infer that this weaker coupling between $\langle\Omega_1^0\rangle$ and $k_{\mathrm{B}}T$ stems from the similarity in size between the probe and the bath ALPs.

Figure 8(b) shows the same data for probe particles with $R_{\mathrm{p}} > 1.0\sigma$ only. They roughly collapse onto one master curve, where $\Delta k_{\mathrm{B}}T$ initially increases linearly, and then quadratically as a function of $|\langle\Omega_1^0\rangle|$. The solid black lines show the corresponding slopes for reference.

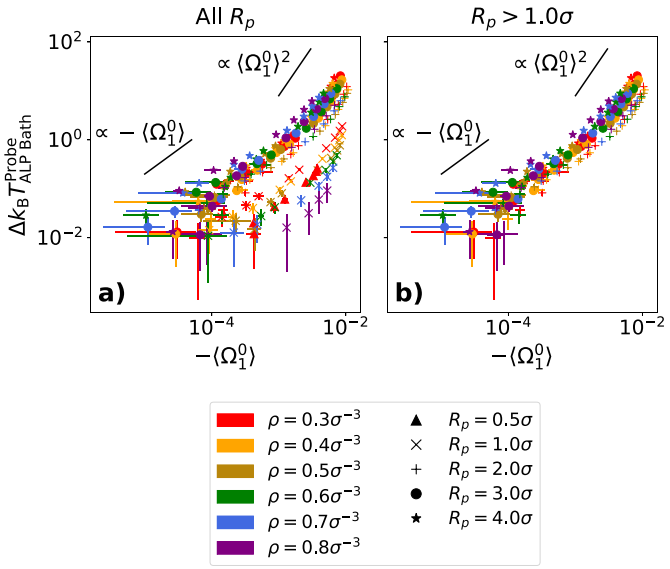

Figure 8. Kinetic temperature difference between the immersed probe and the ALP bath as a function of the average dipole moment, $\langle\Omega_1^0\rangle$, for (a) all radii and (b) for radii $R_\mathrm{p} > 1.0\sigma$. Data for all simulated bath densities (ρ) and activities ($\hat{F}_0$), as well as for all probe radii (R_p), are shown. Different probe radii a distinguished by different symbols and different bath densities are distinguished by different colors. Bath activities are not distinguished.

Overall, this positive correlation shows that the kinetic temperature (and hence the velocity of the probe, and probably active-like behavior as a whole) is mainly driven by the accumulation of particles behind it for larger probe sizes. Based on this positive correlation as well as the fact that the peak of the dipole moment exhibits non-monotonic behavior, we infer that the non-monotonicity of the kinetic temperature stems from the accumulation of particles around, and in particular behind, the probe. To investigate this further, we graph $(-\langle\Omega_1^0\rangle)$ as a function of R_p in figures 9(a) and (b). We see that non-monotonic behavior indeed occurs for $\hat{F}_0 \gtrapprox 2.1$, which matches the results of figure 2 for the non-monotonic behavior of $\Delta k_\mathrm{B} T$ as a function of R_p. For active forces above this value, $|\langle\Omega_1^0\rangle|$ exhibits a maximum around $R_\mathrm{p} \approx 2\sigma$, which is reasonably close, but not identical, to the value $R_\mathrm{p} \approx 3\sigma$ where the maximum of the kinetic energy was observed.

We additionally plot $(-\langle\Omega_1^0\rangle)$ as a function of $\hat{F}_0$ and ρ in figures 9(c) and (d) respectively. Figure 9(c) shows that $|\langle\Omega_1^0\rangle|$ scales approximately quadratically for low values of $\hat{F}_0$ and approximately linearly for high values of $\hat{F}_0$. This scaling is unsurprising given the scaling in figure 8 and that $\Delta k_\mathrm{B} T \propto \hat{F}_0^2$. The crossover from quadratic to linear occurs at $\hat{F}_0 \approx 1$. At $\hat{F}_0 = 1$, the dominant force switches from the thermal forces to the 'pulling,' active forces [19]. We thus infer that this switch in the prominent forcing mechanism evokes the change in scaling.

In figure 9(d), we see that $|\langle\Omega_1^0\rangle|$ decreases with increasing density. As the bath becomes more dense, crowding causes the distribution of ALPs around the probe to become more uniform. Therefore, the net dipole moment becomes less prominent.

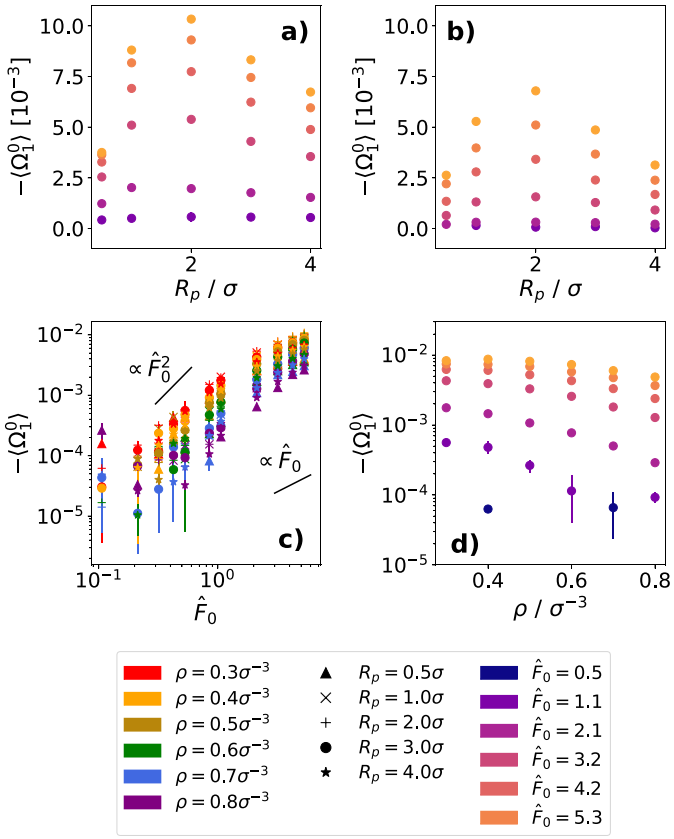

Figure 9. Average dipole moment, $\langle\Omega_1^0\rangle$, as a function of (a)/(b) the radius R_p for a bath of density (c) $\rho = 0.3\sigma^{-3}$, (d) $\rho = 0.8\sigma^{-3}$, (c) the active force of the ALPs $\hat{F}_0$, (d) the density ρ for a probe of radius $R_\mathrm{p} = 3.0\sigma$.

5. Effects of probe inertia

The results of the previous section suggest that the active-particle-like behavior of a probe immersed in an active bath is driven by the accumulation of active particles behind the probe (with respect to its velocity). The extent to which such an accumulation is possible should be influenced by both the size and the mass of the probe particle: Large probe particles offer a larger cross sectional area for interactions with ALPs and accumulation. Massive particles are more inert and change their direction less easily, giving ALPs more time to accumulate in the back. In our simulations so far, we have always kept the mass to volume ratio of the probe constant ($M/\mathcal{V} = 25/(9\pi)m\sigma^{-3}$), which is the most relevant experimental setup corresponding to the neutral buoyant density and thus the absence of sedimentation. In the following, we will study the influence of both factors, mass and size, separately. To this end, we will study the effective temperature of probes for which we keep the probe radius constant at either $R_\mathrm{p} = 0.5\sigma$ or $R_\mathrm{p} = 3.0\sigma$, and vary the probe mass.

In figure 10(a), we see that, when we change the mass of a small probe with radius $R_\mathrm{p} = 0.5\sigma$ within one order of magnitude, the kinetic temperature increases only very slowly with the mass and the difference between the kinetic temperature of the bath ALPs and the probe remains approximately zero. However, once the probe becomes considerably more massive

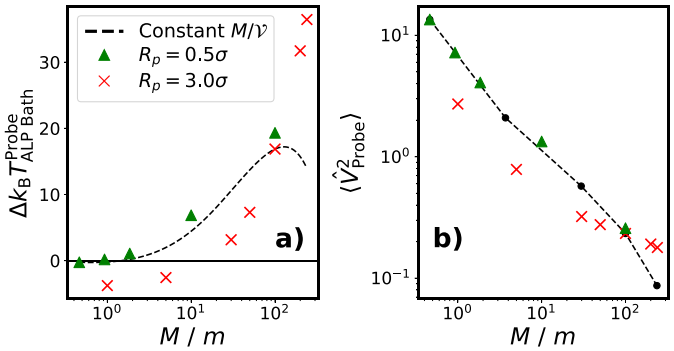

Figure 10. (a) Kinetic temperature difference between the probe and ALP bath in units of $k_B T$ and (b) mean squared velocity of the probe in units of $k_B T/m$ as a function of the probe mass. The ALP bath has density $\rho = 0.4\sigma^{-3}$ and activity $\hat{F}_0 = 5.3$. Red x-markers represent probes where the radius is held constant at $R_p = 3.0\sigma$ regardless of mass. Green triangle markers represent probes where the radius is held constant at $R_p = 0.5\sigma$ regardless of mass. In (a), the dashed black line shows the spline interpolation from figure 2. In (b), black circle markers connected by a dashed line represent probes where the mass to volume ratio is held constant at $M/\mathcal{V} = 25/(9\pi)m\sigma^{-3}$.

than the active particles themselves, we begin to see a significant increase in the probe kinetic temperature. A closer inspection of the local structure (see figure 17(c) in appendix G) shows that the mechanism for this increase in the kinetic temperature is indeed again the accumulation of particles behind the probe. Once the probe becomes sufficiently massive, accumulation is possible even behind small probes because the probe's inertia makes it difficult for the bath ALPs to incite its movement.

We also see in figure 10(a) that the kinetic temperature of a probe with radius $R_p = 3.0\sigma$ and varying mass increases monotonically with increasing mass. This behavior is unlike the non-monotonic behavior that we see for probe particles where the mass to volume ratio is held constant. Additionally, it is interesting to note that for small masses, the kinetic temperature of the small probes is larger than that of the large probes, but it grows more slowly with M, such that the two become comparable at $M \sim 100m$.

To better understand the behavior of the kinetic temperature of the probes, we plot the mean squared velocity as a function of the probe mass in figure 10(b). In accordance with figure 10(a), we see that small probes have higher squared velocities than large probes with the same mass. In both cases, the squared velocity initially decreases roughly as $1/M$ with increasing M (corresponding to roughly constant kinetic temperature), then the curves flatten at around $M/m \sim 10$. The flattening is much more pronounced for large particles than for small particles, such that the two curves meet at $M/m \sim 100$. The slow decay of the mean squared velocity in particular for the large probes of $R_p = 3.0\sigma$ is a strong signature of non-equilibrium behavior and shows that, in this mass range, the dynamics of the particle are primarily determined by the activity of the bath and its interaction with the boundary of the probe, rather than the probe's inertia.

The above investigation of probes with different masses and constant radius reveals that not only the probe volume (surface area), but also the inertia contributes to its acquiring of active-particle-like behaviors. In both cases, this active-particle-like behavior is driven by the accumulation of active particles behind the probe. Based on the observations reported above, we propose the following picture:

First, our results indicate that the effect of the ALP bath on the dynamics of a probe with a *given probe mass* is stronger if the probe is smaller. This holds for both the kinetic temperature (see figure 10(b) for $M/m < 100$) and the amplitude of the ALP accumulation behind the probe (see figure 17 in appendix G). Furthermore, we have seen in section 3 that the effect of the ALP bath is stronger if the bath density is lower. Both observations taken together suggest that the effective boundary forces are mostly determined by the fluctuations of ALP-probe contacts at the boundary surface. For small probe particles and small ALP bath densities, the particle experiences few interactions in a small given time window, and the net force fluctuates strongly. For large probe particles and/or large ALP bath densities, the total number of contacts is large, but the sum of the net transmitted forces averages to a smaller value.

Second, figure 10 suggests the existence of three different regimes of probe boundary interactions. If the probe mass M is small (of order m), the particle is easily shoved around and frequently changes its direction. In this 'quasithermal' regime, random collisions with ALP bath particles lead to an incomplete 'thermalization' of the probe, which is more efficient for small particles than for larger particles. Therefore, larger particles do not quite reach the ALP bath temperature. If M is larger, the particle velocities change more slowly, and bath ALPs start to accumulate at the probe particle. This is stabilized by a positive feedback between the instantaneous particle velocity and the ALP accumulation, whereby the latter pushes the particle in the direction of the former. This 'accumulation' regime is encountered if the inertial time scale of the probe particle is sufficiently large that the positive feedback loop can be sustained, and it is associated with an increase of kinetic temperature. However, positive feedback is only possible if the instantaneous velocity of the particle exceeds a certain critical limit. Once the velocity is too small, a third 'slow particle' regime is entered, where the feedback loop weakens and eventually breaks down.

Within this picture, the nonmonotonic behavior of the kinetic temperature for probe particles with fixed mass to volume ratio ($M/\mathcal{V} = 25/(9\pi)m\sigma^{-3}$) can be rationalized as follows: it results from a subtle interplay of mass and size. Initially, the system is either in the 'thermalization' regime (at $R_\mathrm{p} \sim 0.5\sigma$) or in the 'accumulation' regime (at $R_\mathrm{p} \geqslant 1\sigma$), and the kinetic temperature increases. However, once the size exceeds $R_\mathrm{p} \sim 3\sigma$, the velocity becomes so small due to the size effect that the 'slow particle' regime is entered and the kinetic temperature decreases again. Indeed, figure 10(b) shows that the mean squared velocity of probe particles $R_\mathrm{p} \sim 4\sigma$ drops down to less than $0.1k_\mathrm{B}T/m$.

6. Conclusions and outlook

In sum, we have investigated the mechanism for the active-particle-like behavior of a probe immersed in an active bath. We have shown that this behavior as well as the enhanced kinetic temperature of a probe cannot simply be attributed to the convective motion of the active bath. The impenetrable boundary of the probe contributes significantly to these adopted dynamics. It causes active bath particles to accumulate behind the probe with respect to its instantaneous velocity. Once gathered behind the probe, particles are forced to move in the same direction, leading to correlations among bath particles with sufficiently high activity. This gathering of active bath particles pushes the probe, inducing transient positive feedback which can be seen in the memory kernel. This, in turn, promotes the active-particle-like behavior of the probe, in particular its enhanced kinetic temperature. The enhanced kinetic temperature of the probe in comparison with the active bath particles implies that the results of passive microrhelogical experiments in active systems must be interpreted with care: equilibrium relations between dynamical properties of the probe and the active bath particles may no longer apply. In future

work, it would be interesting to examine whether this temperature difference could be used to design an active heat engine.

These boundary interactions, and consequently the dynamics of both the probe and the active fluid, are highly contingent on the specific configuration of the probe boundary. For probes with a radius approximately equal to that of the bath particles, the accumulation mechanism is significantly less effective. Furthermore, the kinetic temperature difference between the probe and the active fluid is dependent on the probe radius. The variability the boundary interactions furnishes us with another non-equilibrium signature of a probe immersed in an active bath: probes of different sizes acquire different kinetic temperatures, even when immersed in the same active bath.

We additionally found that the kinetic temperature difference between the immersed probe and the active bath scales non-monotonically with the probe size. This non-monotonicity is driven by the accumulation of active particles behind the probe. This accumulation must behave non-monotonically as a function of the probe size: for small probes, the surface area is too low to generate accumulation; for large probes, the probe velocity goes to zero, meaning the accumulation must be uniform.

Because our active particles are coupled to a Langevin thermostat, the hydrodynamic interactions in the fluid are effectively screened. In future work, it would be interesting to study systems with hydrodynamic interactions, which would certainly impact the correlations both within the active fluid and between the active fluid and the passive probe. Furthermore, given the importance of the boundary in both the dynamics of the probe and the active fluid, it would be interesting to consider a boundary with localized deformations. It has been shown that such boundary deformities can induce long-range effects in the bulk active fluid [66], which may in turn alter the dynamics of the immersed probe.

Data availability statement

The data cannot be made publicly available upon publication because they are not available in a format that is sufficiently accessible or reusable by other researchers. The data that support the findings of this study are available upon reasonable request from the authors.

Acknowledgments

This work was funded by the Deutsche Forschungsgemeinschaft (DFG) via Grant 233630050, TRR 146, Project A3. This research was conducted using the supercomputer MOGON 2 offered by Johannes Gutenberg University Mainz (hpc.uni-mainz.de), which is a member of the AHRP (Alliance for High Performance Computing in Rhineland Palatinate, www.ahrp.info) and the Gauss Alliance e.V.. We thank Martin Hanke, Niklas Bockius, and Thomas Speck for useful discussions.

Appendix A. Probe mean squared displacement

For overdamped particles, a signature characteristic of active-particle-like behavior is the crossover of the MSD from the ballistic to the diffusive regime. However, for underdamped particles, this crossover occurs even for passive particles due to their inertia. Because we model both our active bath particles and our immersed probe as being underdamped, we see that in both the case of a passive and an active bath the probe exhibits a crossover from the ballistic

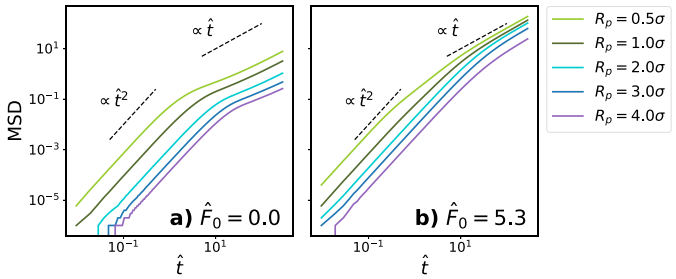

Figure 11. Mean squared displacement of different sized probes immersed in a bath of density $\rho = 0.4\sigma^{-3}$. (a) The mean squared displacement for a passive bath. (b) The mean squared displacement for an active bath with activity $\hat{F}_0 = 5.3$.

to the diffusive regime. Consequently, we cannot use the crossover of the MSD as a signature of active-particle-like behavior. It should, however, be noted that the diffusion coefficient of the probe changes by over two orders of magnitude for the large probes as discussed in appendix C.

Appendix B. Velocity distribution for probes of different sizes

To calculate $P(\hat{\mathbf{v}})$ from our simulation data, we calculate the absolute velocity, $|\mathbf{v}|$, of the particle for each time step. We then assign this value of $|\mathbf{v}|$ to an appropriate bin, each of length dv, to find the absolute velocity distribution $N[|\mathbf{v}|]$. We divide each of these bins by its true volume, $\delta V = \frac{4}{3}\pi\left((v+\frac{dv}{2})^3 - (v-\frac{dv}{2})^3\right)$, and scale the distribution by a factor of $\sqrt{m/k_{\mathrm{B}}T}$ to find $P(\hat{\mathbf{v}})$. The distribution calculated from simulation data is normalized such that $\sum_{|\hat{\mathbf{v}}|} P(\hat{\mathbf{v}})\delta V = 1$. Theoretical distributions of $P(\hat{\mathbf{v}})$ are normalized such that $\int_\infty \mathrm{d}\hat{v}\, 4\pi\hat{v}^2 P(\hat{\mathbf{v}}) = 1$.

In figures 12(a)–(e), we plot the velocity distributions $P(\hat{\mathbf{v}})$, of the different sized probes listed in table 1 in a bath of density $\rho = 0.3\sigma^{-3}$. We also show zero-centered Gaussian distributions with the same standard deviation as the simulation data. At least qualitatively, the Gaussian distributions seem to match the simulation data very well.

To better quantify this deviation from a Gaussian distribution, we calculate the relative entropy (Kullback–Leibler divergence) between the velocity distribution of the probe, as calculated from simulation data, and a zero-centered Gaussian distribution with the same standard deviation. The relative entropy between these two distributions is defined as:

$$D_{\mathrm{KL}}\left(\mathcal{P}\left(\hat{\mathbf{v}}\right)||\mathcal{Q}\left(\hat{\mathbf{v}}\right)\right) = \int_\infty \mathrm{d}^3\hat{v}\,\mathcal{P}\left(\hat{\mathbf{v}}\right)\ln\left(\frac{\mathcal{P}\left(\hat{\mathbf{v}}\right)}{\mathcal{Q}\left(\hat{\mathbf{v}}\right)}\right), \tag{B1}$$

where $\mathcal{P}(\hat{\mathbf{v}})$ is the velocity distribution from simulation data and $\mathcal{Q}(\hat{\mathbf{v}})$ is the reference Gaussian distribution.

This quantity is plotted in figures 12(a′)–(e′). From figures 12(a′)–(e′), we see that the deviations from a Gaussian distribution are generally very small. We do see some relatively large deviations for small probes ($R_{\mathrm{p}} \leqslant 2.0\sigma$) immersed in active baths of low density ($\rho = 0.3\sigma^{-3}$) in figures 12(a′)–(c′). However, when we look at the velocity distributions in figures 12(a)–(c), these deviations are only qualitatively noticeable near $|\hat{\mathbf{V}}| = 0$, where the true volume (δV) goes to zero. Given that we divide by δV to calculate $P(\hat{\mathbf{v}})$, these deviations are likely

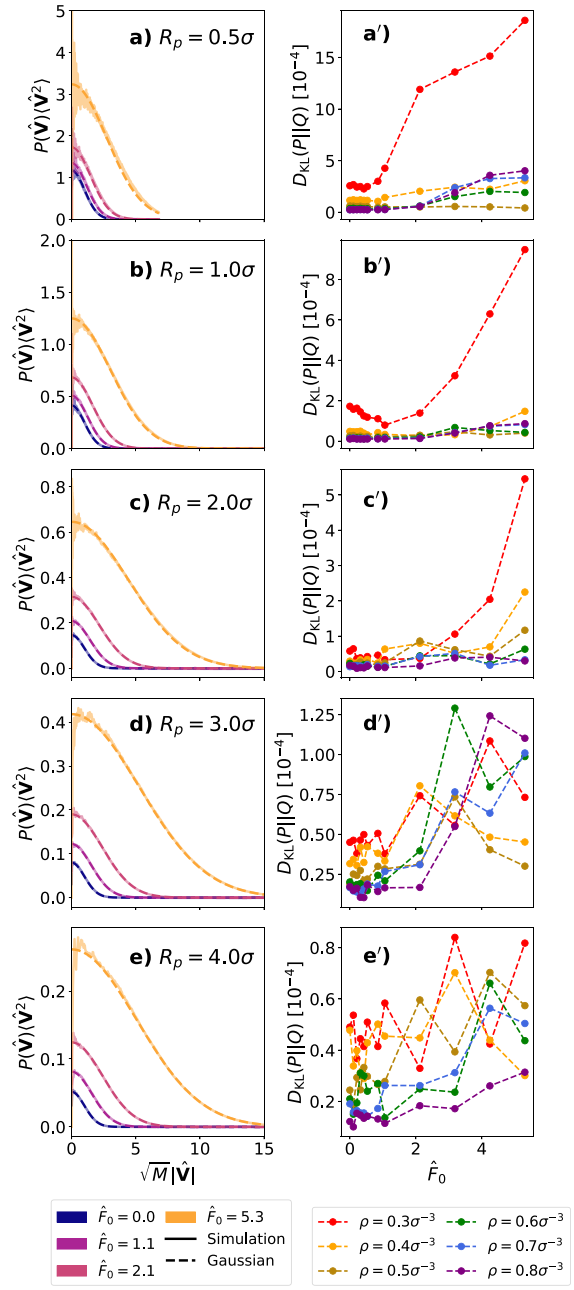

Figure 12. (a)–(e): Velocity distributions of different sized probes immersed in a bath of density $\rho = 0.3\sigma^{-3}$ for different driving forces $\hat{F}_0$. Solid lines show simulation data, whereas dotted lines show zero-centered Gaussian distributions with the same standard deviation for comparison. The x-axis has been rescaled by $\sqrt{M}$ for better visibility and the x-axis has been rescaled by $\langle\hat{\mathbf{V}}^2\rangle$. (a′)–(e′): Corresponding relative entropies (equation (B1)) between the simulation data and Gaussian distributions with the same standard deviation. Each row corresponds to a different sized probe from table 1: (a)/(a′) $R_\mathrm{p} = 0.5\sigma$, (b)/(b′) $R_\mathrm{p} = 1.0\sigma$, (c)/(c′) $R_\mathrm{p} = 2.0\sigma$, (d)/(d′) $R_\mathrm{p} = 3.0\sigma$, and (e)/(e′) $R_\mathrm{p} = 4.0\sigma$. Densities in the legend are expressed in LJ units of σ^{-3}.

due to numerical inaccuracies. We also see the deviations near $|\hat{\mathbf{V}}| = 0$ for larger probes in figures 12(d) and (e).

We attribute the larger values of relative entropy associated with smaller probes to poorer statistics for such systems: because the bath has a low density, the probe experiences fewer collisions with bath particles, which is only exacerbated by the small size of the probe. Therefore, we conclude that the deviations from a Gaussian distribution are due more to the less robust statistics in these systems than a fundamental lack of Gaussianity in the probe velocity distribution.

Appendix C. Probe diffusion coefficient

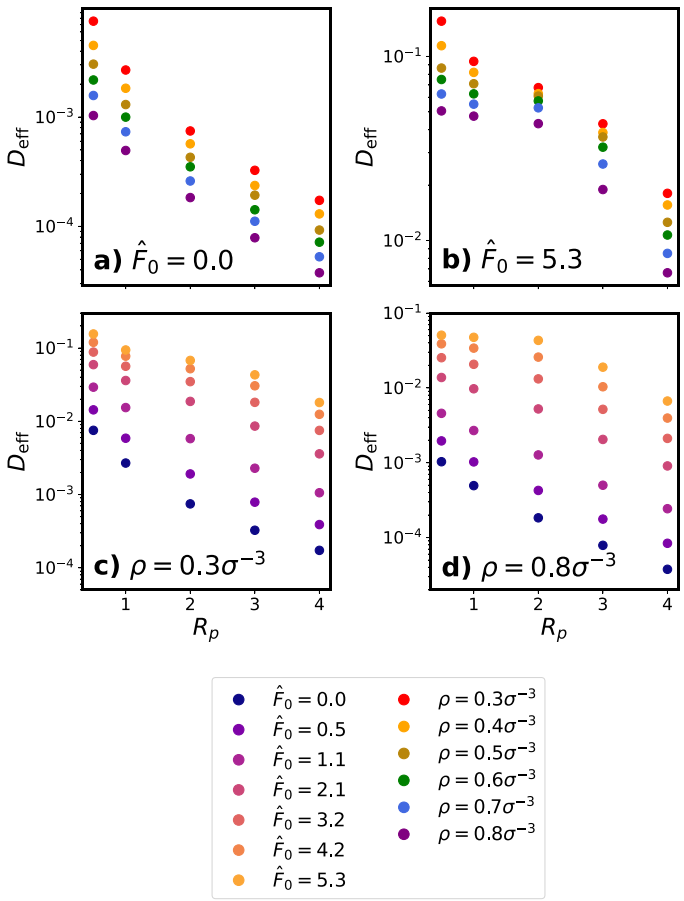

Figure 13. Diffusion coefficient of the probe, D_{eff}, as determined from the velocity autocorrelation function as a function of the probe radius, R_{p}. In the top row, each plot shows ALP baths of different densities (ρ, each a different color) for a (a) passive bath $\hat{F}_0 = 0.0$ and (b) an active bath with activity $\hat{F}_0 = 5.3$. In the bottom row, each plot shows ALP baths of different activities ($\hat{F}_0$, each a different color) for a specific bath density (ρ): (c) $\rho = 0.3\sigma^{-3}$ and (d) $\rho = 0.8\sigma^{-3}$.

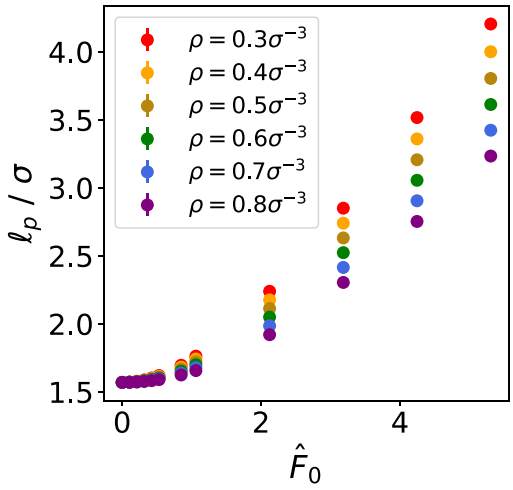

Figure 14. Persistence length of an ALP for different densities (shown as different colors) as a function of the active force $\hat{F}_0$.

From the VACF, we calculate the diffusion coefficient of the immersed probe as:

$$D_{\text{eff}} = \frac{1}{3}\int_0^\infty C_{\text{V}}(t)\,, \tag{C1}$$

where $C_{\text{V}}(t)$ is the VACF. We graph the results of this calculation in figure 13. Unlike the kinetic temperature, we find that, within the parameters that we tested, the diffusion coefficient decreases with particle size and does not exhibit non-monotonic behavior. However, in figures 13(b) and (d) we see that for the highest density and bath activity which we test ($\rho = 0.8\sigma^{-3}$ and $\hat{F}_0 = 5.3$), we observe an emerging plateau at small particle sizes. If we extended to higher activities, it is possible that there may be non-monotonic behavior, at least in high density baths.

Appendix D. Active Langevin particle persistence length

The dynamics of active particles can generally be characterized by two parameters: the speed of propulsion and the rotational diffusion time. These two parameters can be used to define a persistence length during which an active particle travels without reorienting. For an active Brownian particle, this persistence length is typically defined as $\ell_{\text{p}} = v_0/((d-1)D_{\text{R}})$, where v_0 is the propulsion velocity, d is the dimensionality of the system, and D_{R} is the rotational diffusion constant. In analogy with this definition, we define the persistence length of an ALP as:

$$\ell_{\text{p}} = \frac{\sqrt{\langle \mathbf{v}^2 \rangle}}{(d-1)\,D_{\text{R}}}. \tag{D1}$$

We show the ALP persistence length for different densities as a function of $\hat{F}_0$ in figure 14.

From figure 14, we see that $\ell_{\text{p}} > R_{\text{p}}$ at all active forces for probes of $R_{\text{p}} \lesssim 1.5$. This characteristic of the ALPs likely contributes to the qualitatively different behavior we see for probes of radii $R_{\text{p}} = 0.5\sigma$ and $R_{\text{p}} = 1.0\sigma$. Furthermore, ℓ_{p} grows with the active force of the ALPs. In

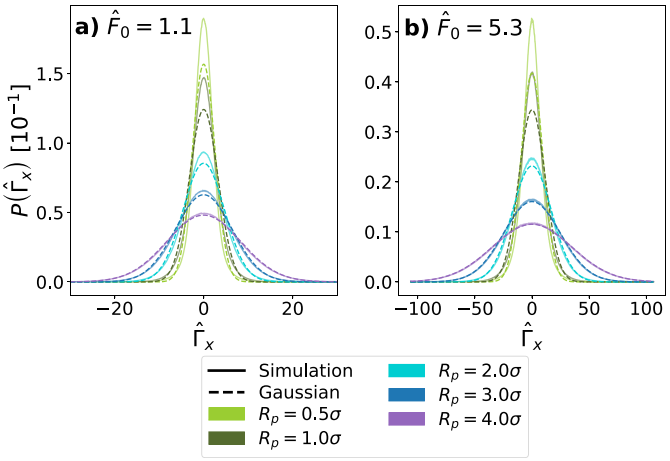

Figure 15. Stochastic force distribution of different sized probes immersed in a bath of density $\rho = 0.4\sigma^{-3}$. The solid lines show simulation data, whereas the dotted lines show zero-centered Gaussian distributions with the same standard deviation. (a) The stochastic force distribution for a bath with activity $\hat{F}_0 = 1.1$. (b) The stochastic force distribution for an active bath with activity $\hat{F}_0 = 5.3$.

section 3.1, we see that the kinetic temperature difference between the probe and the bath ALPs exhibits non-monotonic behavior as a function of probe radius, reaching a maximum at some probe radius $R_{\max}$. We found in section 3.1 that the value of $R_{\max}$ decreases with increasing bath activity (see figure 3(a)); therefore, given the opposite behavior of ℓ_{p} and $R_{\max}$ as function of $\hat{F}_0$, we conclude that the persistence length of the ALPs cannot explain the non-monotonic behavior of the kinetic temperature difference.

Appendix E. Stochastic force distribution

From a trivial rewriting of equation (5), we calculate the stochastic force on the probe particle directly from our simulation data (see figure 15). We find that, for probes of large radii, the stochastic force distribution on the probe is Gaussian, as has previously been shown for a probe of radius $R_{\mathrm{p}} = 3.0\sigma$ [19]. However, it is notable that there are some deviations from a Gaussian distribution for probes with smaller radii. In [19], it has been shown that the stochastic force distribution of an immersed probe exhibits deviations from a Gaussian distribution at low densities, even when the bath is passive. The peaks in the simulation are sharper than the Gaussian distribution. Given this result, we attribute the deviations we see here to small numbers, i.e. few collisions with bath particles, caused by the small size of the immersed probe, such that the central limit theorem no longer applies.

Appendix F. Correlations and density in an active Langevin particle bath

In section 3.1, we saw that the kinetic temperature difference between the probe and the bath ALPs exhibits non-monotonic behavior as a function of probe radius, reaching a maximum at some probe radius $R_{\max}$. We have already shown that the persistence length of the bath ALPs cannot explain this non-monotonic behavior in appendix D. For baths of all densities

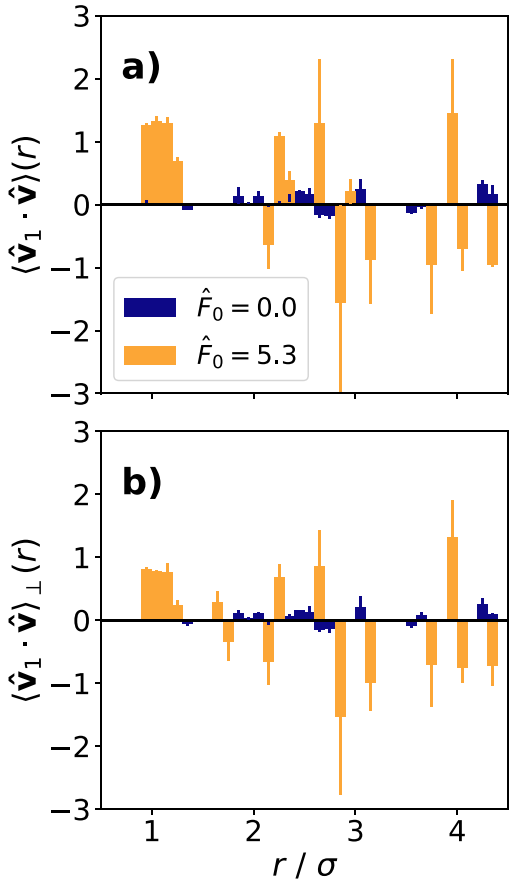

Figure 16. Velocity alignment among active Langevin particles in a bath of global density $\rho_0 = 0.8\sigma^{-3}$. (a) Alignment of ALP velocities with that of a randomly chosen ALP ($\langle \mathbf{v}_1 \cdot \mathbf{v} \rangle (r)$, see equation (10)). (b) Alignment of ALP velocities located on the axis perpendicular to the velocity of a randomly chosen ALP ($\langle \mathbf{v}_1 \cdot \mathbf{v} \rangle_\perp (r)$, see equation (F1)).

and activities, we found the value of $R_{\max} \approx 3\sigma$. Therefore, we would like to assess whether the length 3.0σ somehow characterizes the bath dynamics. Here, we specifically investigate correlations among ALPs.

For the purpose of this investigation, we examine a bath of ALPs (described by equation (1)), absent of the probe. For a single, randomly selected ALP, we then calculate the alignment of other ALPs in the vicinity using equation (10). In equation (10), we simply replace $\mathbf{V}$ with $\mathbf{v}_1$, the velocity of the randomly selected ALP (see figure 16(a)). We are especially interested in correlations between $\mathbf{v}_1$ and the velocities of ALPs which are positioned on the axis perpendicular to $\mathbf{v}_1$. Correlations amongst these perpendicularly located particles would allow for coordinated pushing of the probe. Therefore, in figure 16(b), we specifically examine the quantity:

$$\langle \mathbf{v}_1 \cdot \mathbf{v} \rangle_\perp (r) = \frac{1}{\rho(r)} \sum_{i \in \delta \mathbf{r}} \mathbf{v}_1 \cdot \mathbf{v} \, \frac{|\mathbf{v}_1 \times \mathbf{r}_i|}{|\mathbf{v}_1||\mathbf{r}_i|}, \tag{F1}$$

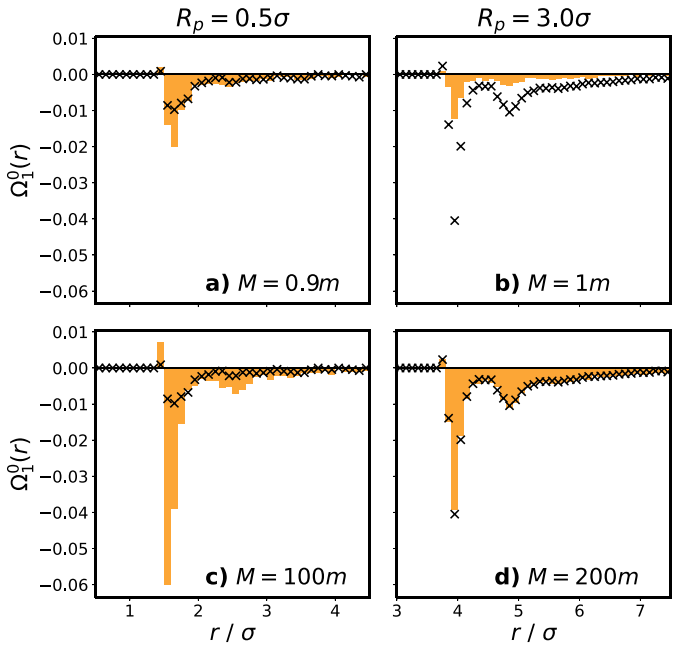

Figure 17. Dipole moment of the bath ($\Omega_1^0(r)$, see equation (8)) for (a) a probe of radius $R_\mathrm{p} = 0.5\sigma$ with mass $M = 0.9m$, (b) a probe of radius $R_\mathrm{p} = 3.0\sigma$ with mass $M = 1m$, (c) a probe of radius $R_\mathrm{p} = 0.5\sigma$ with mass $M = 100m$, and (a) a probe of radius $R_\mathrm{p} = 3.0\sigma$ with mass $M = 200m$. For ease of visualization, we show a black line at 0. Black x-markers represent the data for probes which have the same radius, but for which the mass to volume ratio is $M/\mathcal{V} = 25/(9\pi)m\sigma^{-3}$. The ALP bath has density $\rho = 0.4\sigma^{-3}$ and activity $\hat{F}_0 = 5.3$.

where $\mathbf{r}_i$ is the distance vector from ALP i to the selected ALP.

In agreement with our results in section 4.1, we see that the motion of particles in a passive bath is uncorrelated. In an active bath, we see that the velocities of the ALPs do become correlated, again in agreement with section 4.1. We find these correlations up to a length of $\sim 1.0\sigma$. A significant amount of these correlations are among particles positioned along the axis perpendicular to $\mathbf{v}_1$ (see figure 16(b)). On larger length scales, the ALPs become uncorrelated again. The correlation length scale of $\sim 1.0\sigma$ does not match the value of $R_\mathrm{max} \approx 3.0\sigma$ which we saw in section 3.1. Therefore, these correlations cannot explain such a value of R_max.

Appendix G. Accumulation for probes of different masses

In section 5, we saw that even probes with very small surface areas could acquire enhanced kinetic temperatures. To confirm that accumulation of active particles in the vicinity of the probe remains the mechanism behind this enhanced kinetic temperature, we graph the dipole moment in the vicinity of the probe for a variety of probes with different radii and masses in figure 17. In figure 17(b), we can indeed see that, small probes with large masses can indeed generate accumulation in spite of their lack of surface area. Furthermore, we can see in figure 17(c),

that even if probes have a large surface area, they cannot generate ALP accumulation without sufficient mass. However, we see in figure 17(d) that, once the probe inertia is relatively large, further increasing it does not significantly affect the accumulation.

We note that, the maximum of the negative dipole moment occurs at a different radius for probes of small (left column) vs. large (right column) radii. For larger probes, the maximum occurs at a larger radius than for smaller probes. Therefore, given that in equation (8) the moment is normalized by the volume, larger spheres still have many more ALPs accumulated than small spheres (in absolute numbers).

ORCID iDs

Jeanine Shea https://orcid.org/0000-0003-2248-6155
Gerhard Jung https://orcid.org/0000-0002-6739-1603
Friederike Schmid https://orcid.org/0000-0002-5536-6718

References

[1] Pedley T J and Kessler J O 1992 Hydrodynamic phenomena in suspensions of swimming microorganisms *Annu. Rev. Fluid Mech.* **24** 313–58
[2] Kurtuldu H, Guasto J S, Johnson K A and Gollub J P 2011 Enhancement of biomixing by swimming algal cells in two-dimensional films *Proc. Natl Acad. Sci.* **108** 10391–5
[3] Caspi A, Granek R and Elbaum M 2000 Enhanced diffusion in active intracellular transport *Phys. Rev. Lett.* **85** 5655–8
[4] Wu X L and Libchaber A 2000 Particle diffusion in a quasi-two-dimensional bacterial bath *Phys. Rev. Lett.* **84** 3017–20
[5] Mikhailov A S and Kapral R 2015 Hydrodynamic collective effects of active protein machines in solution and lipid bilayers *Proc. Natl Acad. Sci.* **112** E3639–44
[6] Leptos K C, Guasto J S, Gollub J P, Pesci A I and Goldstein R E 2009 Dynamics of enhanced tracer diffusion in suspensions of swimming eukaryotic microorganisms *Phys. Rev. Lett.* **103** 198103
[7] Ortlieb L, Rafaï S, Peyla P, Wagner C and John T 2019 Statistics of colloidal suspensions stirred by microswimmers *Phys. Rev. Lett.* **122** 148101
[8] Miño G L, Dunstan J, Rousselet A, Clément E and Soto R 2013 Induced diffusion of tracers in a bacterial suspension: theory and experiments *J. Fluid Mech.* **729** 423–44
[9] Kanazawa K, Sano T G, Cairoli A and Baule A 2020 Loopy lévy flights enhance tracer diffusion in active suspensions *Nature* **579** 364–7
[10] Tripathi A K and Tlusty T 2022 Gauging nanoswimmer dynamics via the motion of large bodies *Phys. Rev. Lett.* **129** 254502
[11] Feng M and Hou Z 2021 Effective dynamics of tracer in active bath: a mean-field theory study (arXiv:2110.00279)
[12] Steffenoni S, Kroy K and Falasco G 2016 Interacting brownian dynamics in a nonequilibrium particle bath *Phys. Rev.* E **94** 10
[13] Speck T and Jayaram A 2021 Vorticity determines the force on bodies immersed in active fluids *Phys. Rev. Lett.* **126** 138002
[14] Yan W and Brady J F 2015 The force on a boundary in active matter *J. Fluid Mech.* **785** 1469–7645
[15] Yan W and Brady J F 2018 The curved kinetic boundary layer of active matter *Soft Matter* **14** 279–90
[16] Reichert J and Voigtmann T 2021 Tracer dynamics in crowded active-particle suspensions *Soft Matter* **17** 10492–504
[17] Baek Y, Solon A P, Xinpeng X, Nikola N and Kafri Y 2018 Generic long-range interactions between passive bodies in an active fluid *Phys. Rev. Lett.* **120** 058002
[18] Granek O, Baek Y, Kafri Y and Solon A P 2020 Bodies in an interacting active fluid: far-field influence of a single body and interaction between two bodies *J. Stat. Mech.* 063211

[19] Shea J, Jung G and Schmid F 2022 Passive probe particle in an active bath: can we tell it is out of equilibrium? *Soft Matter* **18** 6965–73
[20] Angelani L, Di Leonardo R and Ruocco G 2009 Self-starting micromotors in a bacterial bath *Phys. Rev. Lett.* **102** 048104
[21] Callegari A and Volpe G 2019 *Numerical Simulations of Active Brownian Particles* (Springer International Publishing) pp 211–38
[22] Bechinger C, Di Leonardo R, Löwen H, Reichhardt C, Volpe G and Volpe G 2016 Active particles in complex and crowded environments *Rev. Mod. Phys.* **88** 045006
[23] Takatori S C, Yan W and Brady J F 2014 Swim pressure: stress generation in active matter *Phys. Rev. Lett.* **113** 028103
[24] Fily Y, Henkes S and Marchetti M C 2014 Freezing and phase separation of self-propelled disks *Soft Matter* **10** 2132–40
[25] Solon A P, Stenhammar J, Wittkowski R, Kardar M, Kafri Y, Cates M E and Tailleur J 2015 Pressure and phase equilibria in interacting active brownian spheres *Phys. Rev. Lett.* **114** 198301
[26] Knežević M and Stark H 2020 Effective Langevin equations for a polar tracer in an active bath *New J. Phys.* **22** 113025
[27] Mallory S A, Valeriani C and Cacciuto A 2014 Curvature-induced activation of a passive tracer in an active bath *Phys. Rev.* E **90** 032309
[28] Yang X, Manning M L and Marchetti M C 2014 Aggregation and segregation of confined active particles *Soft Matter* **10** 6477–84
[29] Berke A P, Turner L, Berg H C and Lauga E 2008 Hydrodynamic attraction of swimming microorganisms by surfaces *Phys. Rev. Lett.* **101** 038102
[30] Li G and Tang J X 2009 Accumulation of microswimmers near a surface mediated by collision and rotational brownian motion *Phys. Rev. Lett.* **103** 078101
[31] Li G, Bensson J, Nisimova L, Munger D, Mahautmr P, Tang J X, Maxey M R and Brun Y V 2011 Accumulation of swimming bacteria near a solid surface *Phys. Rev.* E **84** 041932
[32] Ezhilan B and Saintillan D 2015 Transport of a dilute active suspension in pressure-driven channel flow *J. Fluid Mech.* **777** 482–522
[33] Schaar K, Zöttl A and Stark H 2015 Detention times of microswimmers close to surfaces: Influence of hydrodynamic interactions and noise *Phys. Rev. Lett.* **115** 038101
[34] Duzgun A and Selinger J V 2018 Active brownian particles near straight or curved walls: Pressure and boundary layers *Phys. Rev.* E **97** 032606
[35] Kantsler V, Dunkel J, Polin M and Goldstein R 2013 Ciliary contact interactions dominate surface scattering of swimming eukaryotes *Proc. Natl Acad. Sci. USA* **110** 1187–92
[36] Löwen H 2020 Inertial effects of self-propelled particles: from active brownian to active langevin motion *J. Chem. Phys.* **152** 040901
[37] Takatori S C and Brady J F 2017 Inertial effects on the stress generation of active fluids *Phys. Rev. Fluids* **2** 094305
[38] Scholz C, Jahanshahi S, Ldov A and Löwen H 2018 Inertial delay of self-propelled particles *Nat. Commun.* **9** 5156
[39] Shankar S and Marchetti M C 2018 Hidden entropy production and work fluctuations in an ideal active gas *Phys. Rev.* E **98** 020604(R)
[40] Baskaran A and Marchetti M C 2008 Enhanced diffusion and ordering of self-propelled rods *Phys. Rev. Lett.* **101** 268101
[41] Mandal S, Liebchen B and Löwen H 2019 Motility-induced temperature difference in coexisting phases *Phys. Rev. Lett.* **123** 228001
[42] Das S, Gompper G and Winkler R 2019 Local stress and pressure in an inhomogeneous system of spherical active brownian particles *Sci. Rep.* **9** 6608
[43] Sprenger A R, Jahanshahi S, Ivlev A V and Löwen H 2021 Time-dependent inertia of self-propelled particles: the langevin rocket *Phys. Rev.* E **103** 042601
[44] Shea J, Jung G and Schmid F 2024 Force renormalization for probes immersed in an active bath *Soft Matter* **20** 1767–85
[45] Weeks J D, Chandler D and Andersen H C 1971 Role of repulsive forces in determining the equilibrium structure of simple liquids *J. Phys. Chem.* **54** 5237–47
[46] Plimpton S 1995 Fast parallel algorithms for short-range molecular dynamics *J. Comput. Phys.* **117** 1–19
[47] Puglisi A, Sarracino A and Vulpiani A 2017 Temperature in and out of equilibrium: a review of concepts, tools and attempts *Phys. Rep.* **709–710** 1–60

[48] Loi D, Mossa S and Cugliandolo L F 2008 Effective temperature of active matter *Phys. Rev.* E **77** 051111
[49] Petrelli I, Cugliandolo L F, Gonnella G and Suma A 2020 Effective temperatures in inhomogeneous passive and active bidimensional brownian particle systems *Phys. Rev.* E **102** 012609
[50] Caprini L and Marini Bettolo Marconi U 2020 Active matter at high density: velocity distribution and kinetic temperature *J. Chem. Phys.* **153** 184901
[51] Patteson A E, Gopinath A, Purohit P K and Arratia P E 2016 Particle diffusion in active fluids is non-monotonic in size *Soft Matter* **12** 2365–72
[52] Izvekov S 2013 Microscopic derivation of particle-based coarse-grained dynamics *J. Chem. Phys.* **138** 134106
[53] Klippenstein V, Tripathy M, Jung G, Schmid F and van der Vegt N 2021 Introducing memory in coarse-grained simulations *J. Phys. Chem.* B **125** 4931
[54] Kinjo T and Hyodo S 2007 Equation of motion for coarse-grained simulation based on microscopic description *Phys. Rev.* E **75** 051109
[55] Jung G and Schmid F 2021 Fluctuation-dissipation relations far from equilibrium: a case study *Soft Matter* **17** 6413–25
[56] Izvekov S 2021 Mori-zwanzig projection operator formalism: particle-based coarse-grained dynamics of open classical systems far from equilibrium *Phys. Rev.* E **104** 024121
[57] Vroylandt H 2022 On the derivation of the generalized langevin equation and the fluctuation-dissipation theorem *Europhys. Lett.* **140** 62003
[58] Netz R R 2023 Derivation of the non-equilibrium generalized langevin equation from a generic time-dependent hamiltonian (arXiv:2310.00748)
[59] Abbasi A, Netz R R and Naji A 2022 Non-markovian modeling of non-equilibrium fluctuations and dissipation in active viscoelastic biomatter (arXiv:2207.11307)
[60] Zwanzig R 2001 *Nonequilibrium Statistical Physics* (Oxford University Press)
[61] Mori H 1965 Transport, collective motion and Brownian motion *Prog. Theor. Phys.* **33** 423–55
[62] Zwanzig R 1961 Memory effects in irreversible thermodynamics *Phys. Rev.* **124** 983–92
[63] Shin H K, Kim C, Talkner P and Lee E K 2010 Brownian motion from molecular dynamics *Chem. Phys.* **375** 316–26
[64] Carof A, Vuilleumier R and Rotenberg B 2014 Two algorithms to compute projected correlation functions in molecular dynamics simulations *J. Chem. Phys.* **140** 124103
[65] Knežević M, Podgurski L and Stark H 2021 Oscillatory active microrheology of active suspensions *Sci. Rep.* **11** 22706
[66] Ben Dor Y, Sunghan R, Kafri Y, Kardar M and Tailleur J 2022 Disordered boundaries destroy bulk phase separation in scalar active matter *Phys. Rev.* E **105** 044603